UC San Diego

UC San Diego Electronic Theses and Dissertations

Title

Efficient Sub-Bandgap Light Absorption and Signal Amplification in Silicon Photodetectors

Permalink

https://escholarship.org/uc/item/8kt1j5p4

Author

Liu, Yu-Hsin

Publication Date

2016

Peer reviewed|Thesis/dissertation

eScholarship.org Powered by the California Digital Library
University of California

UNIVERSITY OF CALIFORNIA, SAN DIEGO

Efficient Sub-Bandgap Light Absorption and Signal Amplification in Silicon Photodetectors

A dissertation submitted in partial satisfaction of the
requirements for the degree
Doctor of Philosophy

in

Materials Science and Engineering

by

Yu-Hsin Liu

Committee in charge:

Professor Yu-Hwa Lo, Chair
Professor Prabhakar Bandaru
Professor Shadi Dayeh
Professor Shaya Fainman
Professor Andrew Kummel

2016

Copyright

Yu-Hsin Liu, 2016

All rights reserved.

The Dissertation of Yu-Hsin Liu is approved, and it is acceptable in quality and form for publication on microfilm and electronically:

_____

_____

_____

_____

_____
Chair

University of California, San Diego

2016

DEDICATION

To my family and loved ones…

TABLE OF CONTENTS

LIST OF FIGURES

LIST OF TABLES

ACKNOWLEDGMENTS

This dissertation would not have been possible without the help and support from many people. First, I would like to thank my advisor, Prof. Yu-Hwa Lo for his guidance on my doctorial researches, including theoretical calculations, device simulation, process and mask designing, fabrication, measurements and analysis. Joining his research group is really an important point through my career. I've learnt a lot from him not only for technical aspects but also the way to analyze and solve problems. I especially appreciate his guidance on the physical modeling and formulations for the device mechanism. This training makes me realize the importance of the mathematics and the programming as an engineer, which were the weakest parts of my formal education in Taiwan. I also want to thank him for the trainings on my presentation skills and attitudes. He spent a lot of time on me for practicing talks every time I went to conferences or had meetings with collaborators. He is not only a good researcher but also really a wonderful educator with patient and enthusiasm. It has been a great pleasure and honor working with him for the last five more years.

Next, I would like to thank my dissertation committee members, Prof. Prabhakar Bandaru, Prof. Shadi Dayeh, Prof. Shaya Fainman, and Prof. Andrew Kummel for their time, interest, and valuable comments about my research. They gave me many suggestions on my projects and also lend me the equipments for some measurements in the dissertation.

I would also like to thank Prof. Lu Jeu Sham for his guidance on physical modeling for the cycling excitation process. He has always been interested in my experimental results and gave valuable comments for the device mechanism.

I want to thank Prof. Peter Asbeck and Prof. Gabriel Rebeiz for their time and comment on my noise measurements and also lend me the equipments. I also thank Prof. Yuan Taur and Prof. S.S. Lau for the supporting on teaching assistant works.

Next, I want to thank my mentor in the group, Dr. James Cheng, who taught me and helped me a lot when I just joined the group with no knowledge on simulation and optical setup, and barely experiences on fabrication. He is really patient and always indicate me the tools and methods I could use for my researches. I also thank my labmate, Dr. Yuchun Zhou, who joined the group around the same time as me. We had worked on many projects together, from Intel, Illumina, to Nano3, we learnt and supported each other and he taught me many things at the beginning.

I want to thank my group members in photonics: David Hall, Alex Zhang, Lujiang Yan, Iftikhar Ahmad Niaz, Mahmut S. Kavrik, and Mohammad Raihan Miah. They really helped me a lot on device measurements and physical model formulations. They are always willing to help and discuss, I’ve learnt a lot from them. I also appreciate other former group members, Dr. Samia Rahman, Dr. Hongkwon Kim, Dr. Hassan Faraby and Yi-Che Chen for their help and support for all the projects.

I’d like to thank my parents, Cheng-Huang Liu and Tseng-Hung Yen, who always support my choice and be proud of my works; my younger brother, Yu-Chi Liu, for his friendship and taking care of my family in Taiwan. I also appreciate all the caring and supports from all family members, both in Taiwan and in U.S.

I’d like to specially thank my husband, Chih-Hsaing Ko, for his understanding, caring, and accompanying. I am so happy that I met him in 2011 and he really fulfills my Ph.D. life.

There are other people in Prof. Lo’s group, who are either currently in the group or graduated, that I would like to acknowledge here for their support and friendship: Yu-Jui (Roger) Chiu, Ramkumar Subramanian, Tiantian Zhang, Tony Minghung Yen, Yuanyuan (Kathy) Han, Ping-Wei Chen, Wei Cai, Jill Tsai, Yugang Yu, Yuesong Shi, Yi Gu. Tsung-Feng Wu, Sung Hwan Cho**,** Zhe Mei, and Wen Qiao.

Last but not least, I want to thank all my friends in the US and Taiwan: Taiwanese friends in UCSD were accompanying me when I came alone and was not familiar with the US. They introduced me to more friends and sometimes helped me on researches as well; all the friends in Taiwan who always sent me a caring messages and shared with me the news in my hometown.

The material in this dissertation is based on the following papers which are published.

Portion of Chapter 2, 3 have been published in Applied Physics Letter 2013, "High efficiency silicon 1310 nm detector without defect states or heteroepitaxy," by

Yu-Hsin Liu, Yuchun Zhou, and Yu-Hwa Lo. The dissertation author was the primary investigator and author of this paper.

Portion of Chapter 4, 5 have been published in Applied Physics Letter 2015, "An Ultra Efficient, Internally Regulated Signal Amplification Mechanism for Light Detection in Semiconductors," by Yu-Hsin Liu, Lujiang Yan, Alex Zhang, David Hall, Iftikhar Ahmad Niaz, Yuchun Zhou, L. J. Sham, and Yu-Hwa Lo. The dissertation author was the primary investigator and author of this paper.

Yu-Hsin Liu

La Jolla, CA

March 2016

VITA

EDUCATION

2004 – 2007	B.S. Materials Science and Engineering, National Tsing Hua University, Taiwan
2007–2009	M.S. Materials Science and Engineering, National Tsing Hua University, Taiwan
2010 – 2016	Ph. D. Materials Science and Engineering Program, University of California, San Diego, USA

PUBLICATIONS

David Hall, Yu-Hsin Liu, and Yu-Hwa Lo, "Single photon avalanche detectors: prospects of new quenching and gain mechanisms", Nanophotonics. 4, 397, 2015.

David Hall, Baoxia Li, Yu-Hsin Liu, Lujiang Yan, and Yu-Hwa Lo, " Complementary metal-oxide-semiconductor compatible 1060 nm photodetector with ultrahigh gain under low bias", Optics Letters. 40, 19 2015.

Yu-Hsin Liu, and Yu-Hwa Lo, "An Ultra Efficient, Internally Regulated Signal Amplification Mechanism for Light Detection in Semiconductors", oral presentation, IEEE Photonics Conference, Reston, (USA), Oct 4-8, 2015.

Yu-Hsin Liu, Lujiang Yan, Alex Zhang, David Hall, Iftikhar Ahmad Niaz, Yuchun Zhou, L. J. Sham, and Yu-Hwa Lo, "Cycling Excitation Process: An Ultra Efficient and Quiet Signal Amplification Mechanism in Semiconductor", Appl. Phys. Lett. 107, 053505, 2015.

Yuchun Zhou, Yu-Hsin Liu, Samia N. Rahman, David Hall, L. J. Sham and Yu-Hwa Lo, "Discovery of a photoresponse amplification mechanism in compensated PN junctions", Appl. Phys. Lett. 106,031103, 2015.

Yu-Hsin Liu, Yuchun Zhou, Yu-Hwa Lo, "High efficiency silicon 1310 nm detector without defect states or heteroepitaxy", Appl. Phys. Lett. 103, 041119, 2013.

Yu-Hsin Liu, Yuchun Zhou, Yu-Hwa Lo, "Efficient Detection of 1310 nm Light Using Silicon Nanoscaled p/n Junctions", oral presentation, IEEE Photonics Conference, Bellevue, (USA), Sept 8-12, 2013.

Yuchun Zhou, Yu-Hsin Liu, James Cheng, YH Lo, "Bias Dependence of Sub-Bandgap Light Detection for Core-Shell Silicon Nanowires", Nano Letters, 12, 5929 , 2012.

ABSTRACT OF THE DISSERTATION

Efficient Sub-Bandgap Light Absorption and Signal Amplification in Silicon Photodetectors

by

Yu-Hsin Liu

Doctor of Philosophy in Materials Science and Engineering

University of California, San Diego, 2016

Professor Yu-Hwa Lo, Chair

This thesis focuses on two areas in silicon photodetectors, the first being enhancing the sub-bandgap light absorption of IR wavelenghts in silicon, and the second being intrinsic signal amplification in silicon photodetectors. Both of these are achieved using heavily doped p-n junction devices which create localized states that relax the k-selection rule of indirect bandgap material. The probability of

transitions between impurity band and the conduction/valence band would be much more efficient than the one between band-to-band transition.

The waveguide-coupled epitaxial p-n photodetector was demonstrated for 1310 nm wavelength detection. Incorporated with the Franz-Keldysh effect and the quasi-confined epitaxial layer design, an absorption coefficient around 10 cm^{-1} has been measured and internal quantum efficiency nearly 100% at -2.5V.

The absorption coefficient is calculated from the wave function of the electron and hole in p-n diode. The heavily doped impurity wave function can be formulated as a delta function, and the quasi-confined conduction band energy states, and the wave function on each level can be obtained from the Silvaco software. The calculated theoretical absorption coefficient increases with the increasing applied bias and the doping concentration, which matches the experimental results.

To solve the issues of large excess noise and high operation bias for avalanche photodiodes based on impact ionization, I presented a detector using the Cycling Excitation Process (CEP) for signal amplification. This can be realized in a heavily doped and highly compensated Si p-n junction, showing ultra high gain about 3000 at very low bias (<4 V), and possessing an intrinsic, phonon-mediated regulation process to keep the device stable without any quenching device required in today's Geiger-mode avalanche detectors.

The CEP can be formulated with the rate equations in conduction bands and impurity states. The gain expression, which is a function of the primary photocurrent

and related to the phonon absorption time, predicts the same trend of the gain increasing with temperature and decreasing with increasing primary photocurrent.

Chapter 1 Silicon Photodetectors

1.1 Photodetectors

The principle of photodetection is based on three processes, photon absorption, photocurrent generation, and carrier transportation. These processes also related to noise generation, sensitivity, gain, and the most important merit, quantum efficiency (or responsivity) of the devices. Briefly, responsivity and quantum efficiency determine how well light is transformed into electrical signal at particular wavelength; gain determines how much the incoming light signal is amplified by multiplication of the detector. In the following sessions, we introduce three types of devices: photoconductors, photodiodes, and avalanche photodiodes[1-3], and discuss the main issues for using these devices.

1.1.1 Photoconductors

A simple photo conductor with length l, electrode surface area A, and an external bias voltage V is shown in Fig.1.1. Constant light illuminates on the device and the electron-hole (e-h) pairs would be generated by photo excitation. Assuming that there is p-type semiconductor device in Fig. 1.1, the photocurrent can be expressed as,

$$\Delta I = q(\mu_n + \mu_p)G_0\tau_n \frac{AV}{l} \cong q\mu_n G_0\tau_n \frac{AV}{l} \tag{1.1}$$

Where μ_n, μ_p are the mobility of electron and hole, usually $\mu_n >> \mu_p$, G_0 is the net optical generation rate, τ_n is the electron lifetime before recombining with a hole. The transit time τ_t of electron is related to the device length and the external bias voltage by,

$$\Delta I = q(G_0 Al)\frac{\tau_n}{\tau_t} \tag{1.2}$$

Where the ratio $\frac{\tau_n}{\tau_t}$ gives the photoconductive gain, which is determined by how fast the electron can travel to the electrode before recombining with the majority holes.

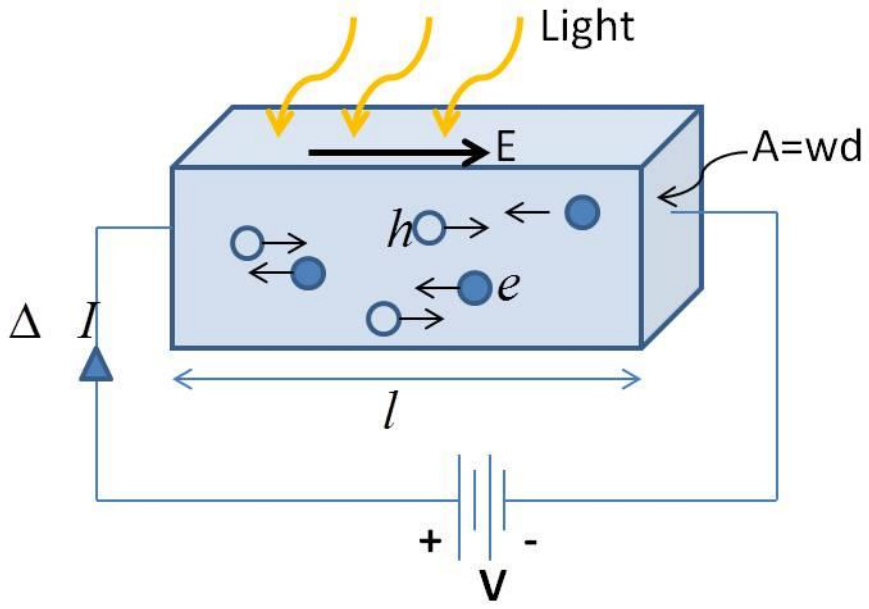

Figure 1.1: Schematic diagram of semiconductor bulk photoconductor[4].

In order to increase the recombination life time of the photo-generated carriers, the superlattice structures[5-6] have been used in the photoconductors as shown in Fig. 1.2. Because of the space charge potential of the ionized impurities, the superlattice potential which modulates the conduction and valence band edges, $E_c(z)$ and $E_v(Z)$. The only way for the electrons and holes to recombine is by lateral tunneling through their barriers. However, in the absence of the electric field, the probability of such tunneling is very small and therefore the recombination rate is drastically reduced.

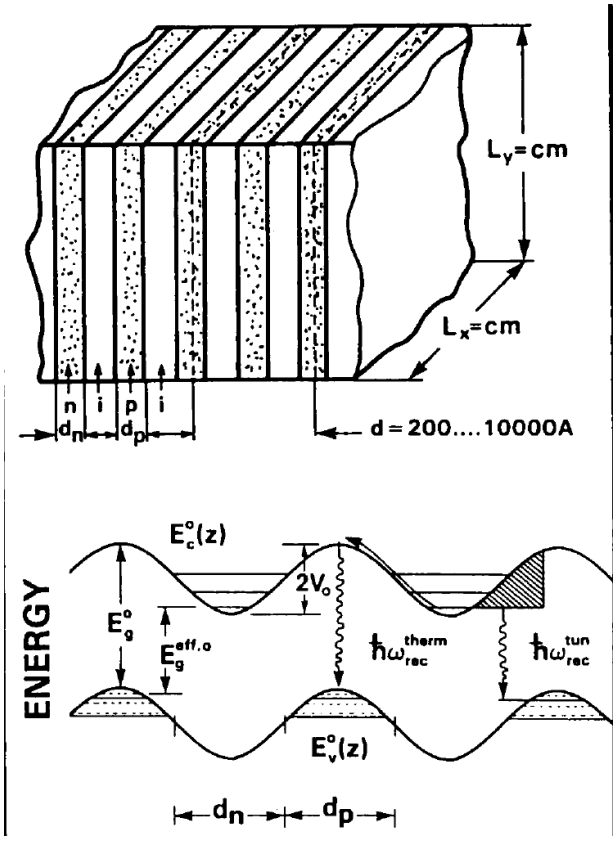

Figure 1.2: Schematic real-space picture and band diagram of a n-i-p-i doping superlattice.

1.1.2 Photodiodes

A photodiode is basically a p-n junction operated under reverse bias. The depletion region serves to separate the photogenerated e-h pairs and the total current I can be written as,

$$I = I_0(e^{qV/k_BT} - 1) - qAG_0(L_p + L_n) \tag{1.3}$$

Where

$$I_0 = qA(\frac{D_p}{L_p} p_{n0} + \frac{D_n}{L_n} n_{p0}) \tag{1.4}$$

is the diode reverse bias current. The last term, $-qAG_0(L_p + L_n)$ is the photocurrent of the diode, which is proportional to the generation rate of the e-h pairs, G_0. L_p, L_n are the diffusion lengths of hole and electron. A is the cross-sectional area of the diode. The absorbed photons produce e-h pairs and these carriers in the depletion region are accelerated in opposite directions and contribute to the photocurrent, the magnitude of which depends on the quantum efficiency.

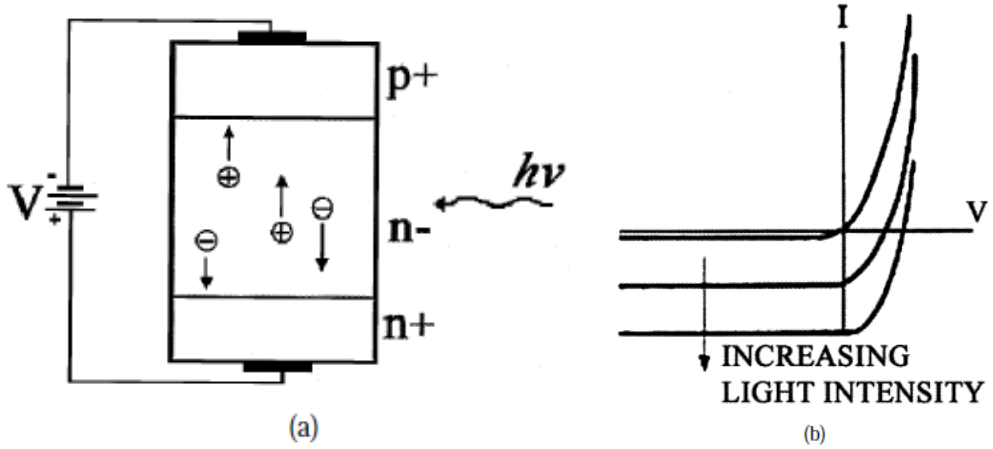

Figure 1.3: Schematic diagram of a p-i-n photodiode[7].

As shown in the equations above, the carrier diffusion length is critical for the device performance. When the depletion region is wide, the greatest amount of light will be absorbed, however, the transit time effect will limit the frequency response if the depletion region is too wide. It also should not be too thin or excessive capacitance C will result in a large RC time constant, where R is the load resistance.

The depletion region thickness is tailored in p-i-n photodiode for optimizing the quantum efficiency. An intrinsic layer is added as the major absorption region as shown in Fig. 1.3.

1.1.3 Avalanche Photodiodes

An avalanche photodiode is a reverse biased p-n junction device operated at a voltage close to the breakdown voltage. An ionization collision with the lattice can occur if the photogenerated primary carriers acquire enough energy. The electrical field to produce the collision is in the range of 10^4 to 10^5 V/cm, depending on the materials. Secondary e-h pairs are produced and drift together with the primary carrier, these may produce more new carriers on the way across the depletion region. This process is known as impact ionization and is illustrated in Fig. 1.4. The avalanche multiplication gain is given by,

$$M = \frac{\left[1-\frac{\alpha_p}{\alpha_n}\right]\exp\left[\alpha_n W\left(1-\frac{\alpha_p}{\alpha_n}\right)\right]}{1-\left(\frac{\alpha_p}{\alpha_n}\right)\exp\left[\alpha_n W\left(1-\frac{\alpha_p}{\alpha_n}\right)\right]} \tag{1.5}$$

Where W is the depletion region width, and

$$\alpha_p(E) = \alpha_{p0} e^{-C_p/E}$$

$$\alpha_n(E) = \alpha_{n0} e^{-C_n/E} \tag{1.6}$$

are the ionization coefficients of the hole and electron, both are functions of the applied electric field E.

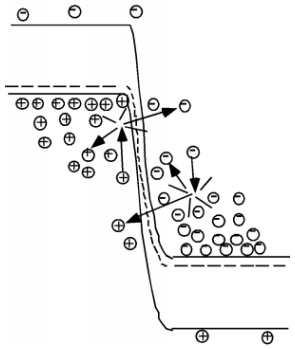

Figure 1.4: Schematic diagram of avalanche multiplication process.

Although the avalanche photodiodes exhibit internal current gain, the additional noise, avalanche noise, comes from the random nature of the avalanche multiplication process in which every e-h pair generated at a given distance in the depletion region does not experience the same multiplication. An excess-noise factor is defined for the multiplication gain M, which is treated as a random variable,

$$F(M) = \frac{\langle M^2 \rangle}{\langle M \rangle^2} \tag{1.7}$$

The excess-noise factor F versus the multiplication gain M plot[8] is obtained based on McIntyle's model[9] . Fig. 1.5 shows that for different values of the ratio of the electron and hole ionization coefficients, the excess-noise factor increases with increasing α_p / α_n ratio for electron injection. For the Si material, in which k_{eff}=0.02,

the excess noise factor increases from 4 to 20, if the multiplication gain increases from 100 to 1000.

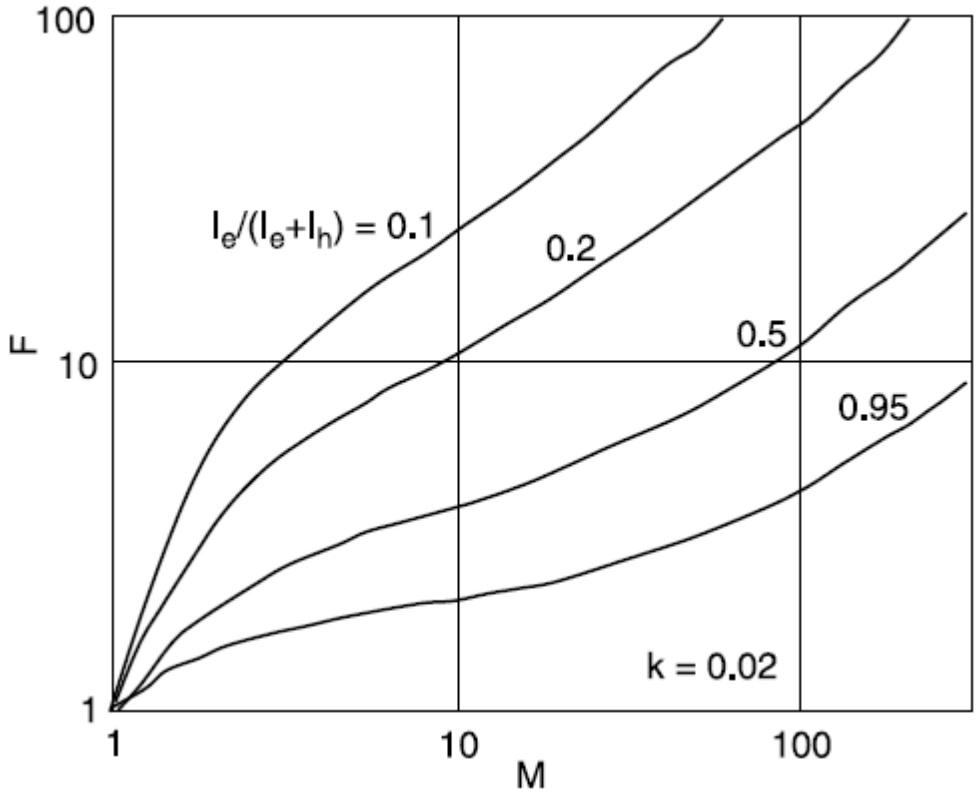

Figure 1.5: Electron-injection-ratio dependence of excess-noise factor *F* as a function of multiplication factor *M*, where *k* = 0.02[10].

1.1.4 Noise of the Devices

In photoconductor devices, the noise is principally generated by the high dark current of the device and is known as Johnson or thermal noise, that has its origins in the random motion of carriers that contribute to the current. The noise current, i_j, is formulated as,

$$\bar{i}_j^2 = \frac{4k_B TB}{R_c} \tag{1.8}$$

Where B is the bandwidth of the device and R_c is the resistance of the photoconducting channel.

The generation-recombination noise current is another source that causes the fluctuations in the carrier concentrations. The noise current is given by,

$$\bar{i}_{GR}^2 = \frac{4q\Gamma_G I_0 B}{1+\omega^2\tau^2} \tag{1.9}$$

This is also called shot noise, which can be reduced if the devices are operated at low temperature. For the diode devices, which are operated at reverse bias voltage with much smaller dark current, the shot noise is only caused in the depletion region.

At very low frequencies, less than 1 kHz, flicker noise arises from surface and interface defects and traps in the bulk of the semiconductor. The spectral noise current is given by,

$$\bar{i}_f^2 \propto \frac{1}{f} \tag{1.10}$$

1.2 Si photodetectors

Silicon is a common material which has been used in electrical or optical devices for a long time. Since the bandgap energy of Si is 1.1 eV, the material only has high absorption coefficient in the visible wavelength range. People usually use

defect impurity to achieve the IR light absorption, however it's difficult to control and not repeatable.

Single photon detection is the ultimate target for photodetectors. Traditionally, impact ionization has been used in the device as an internal gain mechanism. To achieve the enormous magnitude of amplification, the detector usually has to be biased above its breakdown voltage, the voltage at which infinite gain is achieved under DC condition.

In the following session, we will introduce the state of the art techniques of Si IR detectors and also the avalanche photodiodes (APD)

1.2.1 Si IR Photodetectors

In order to reach the sub-bandgap light absorption, other than heteroepitaxial growth (e.g., Ge on Si)[10-11] and heterointegration using wafer bonding (e.g. InP on Si)[12], defect incorporation into the silicon lattice has been a method to achieve this goal. Different defect states applications including mid-bandgap absorption (MBA), surface-state absorption (SSA), and the internal photoemission absorption (IPA) were proposed[13].

Si^+ implantation has been used for creating the midgap states, which enable the sub-bandgap light absorption for Si. Fan[14] had reported that radiation damage Si would produce a photocurrent when illuminated with sub bandgap light. Two crystal defects, divacancies and interstitial clusters, are responsible for this photoresponse. The divacancies are known to anneal out between 100 and 300℃ while the clusters

are stable to >600℃[15]. By ion implantation of Si^{+} 1×10^{13} cm^{-2} at 190 keV into the waveguide increases the optical absorption from 2-3 dB/cm to 80 dB/cm. A Si waveguide photodetectors with ion implantation with responsivity around 0.8 A/V at 5 V has been reported[16].

To increase light interactions with the defect states, structures that maximize the surface area such as nanowires[17-19], very long waveguides[16,21-22], and resonance structures[23-26] have been explored.

By using the interface of semiconductor and metal, the Schottky-barrier-based devices can absorb the photon with energy lower than the semiconductor bandgap. Si waveguide devices integrated with Cu and Ni have been reported, with responsivity 0.08 mA/W at a wavelength of 1550 nm[27-28].

1.2.2 Si Avalanche Photodetectors

In order to achieve the reduction of dark current in APD, uniform carrier multiplication over the whole photosensitive area is required. The defect in the device would cause earlier breakdown than in the junction area, which needs to be avoided during the fabrication process.

On the other hand, the dark current is also contributed from the generation-recombination in the depletion region, leakage current, and tunneling current. Incorporating a guard ring in the Si diode is a common technique to avoid the leakage current around the junction edge[29-32]. The guard ring is an n-p junction

around the periphery of the diode formed by the selective diffusion as shown in Fig. 1.6.

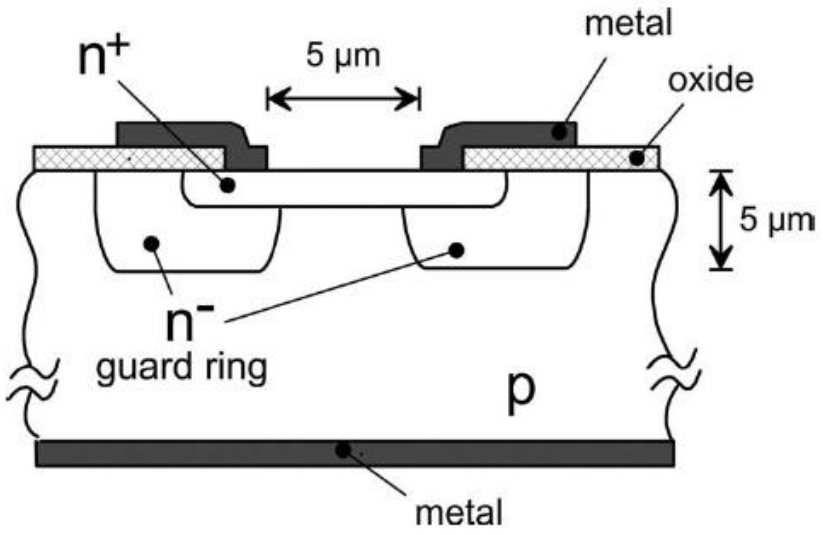

Figure 1.6: The guard ring structure in Si APD to prevent the leakage current around the junction corner.

However, the guard ring structure reduces the detection efficiency. Another design, reach-through APD, can avoid breakdown in the neutral region by extending the depletion region. The absorption region in a lightly doped layer is separated from the multiplication region in heavily doped layer[32-33]. Thin film Si detectors also came into favor due to the lower operating bias and reduced carrier diffusion length. The active area is defined by the center top highly doped p region, and another p+ region at the center layer is used for enhancing the electric field while also providing a low resistivity path for the avalanche current[34]. Photo detection efficiency around 10%~

50% between 540 nm to 800 nm wavelength at reverse bias 20 V has been reported for thin film Si APDs.

1.3 Motivation

Although the defect states inside the bulk or on the surface are effective for sub-bandgap light absorption. However they are not easy to control and unstable for the operation. We have been looking for a method without implantation defects for enhancing the absorption coefficient at IR wavelength for Si material.

Avalanche photodetectors need to be biased to close to the breakdown voltage (> 20 V), and accompany with excess noise amplified with the signal gain. A new mechanism for signal amplification with low operated bias and lower noise is in demand for the applications such as imaging and sensing.

1.4 Synopsis of Dissertation

To enhance the absorption coefficient of Si material at IR wavelength and also investigate the other mechanism for amplifying the photo-generated carriers, the unique heavily doped p-n diode devices are discussed in the following chapters.

In Chapter 2, a waveguide coupled IR detector is introduced. Without the defect states, 1310 nm light absorption coefficient around 10/cm is demonstrated by using the structure design considering Franz-Keldysh effect, quasi-2D confinement, and heavily doping concentration to relax the k-selection rule.

In Chapter 3, the mechanism of the sub-bandgap light absorption for the device in Chapter 2 is formulated into the first principle calculations. The absorption coefficient can be formulated into a function of doping concentration, device size, and bias voltage application.

In Chapter 4, a device design with a compensated doped p-n junction is introduced. The mechanism of cycling excitation process is illustrated, and the Bias and temperature dependence photoresponse for 635 nm wavelength are characterized.

In Chapter 5, the cycling excitation process can be formulated into rate equations. The primary current dependence gain property is shown and which is matched with the experimental results in Chapter 4.

In Chapter 6, a conclusion of using a heavily doped p-n junction device is shown. The future works on cycling excitation process are also presented.

Chapter 2 Heavily Doped Impurity Assisted IR Absorption

2.1 Overview

The Si community has continued to seek low cost, fully complementary metal-oxide-semiconductor (CMOS) compatible optical detection techniques to overcome the interconnect bottleneck facing the electronics world. Here I demonstrate high internal quantum efficiency 1310 nm detectors using entirely the properties of Si crystal by employing homojunction band structure engineering to tailor the optoelectronic properties of the material. Nearly 100% internal detector quantum efficiency has been obtained. The device concept may find broad applications benefiting from the extended spectral response beyond the limit of bandgap, especially the limit associated with indirect bandgap of the material.

2.2 Physical Mechanism

Inspired by the infrared detector of type-II quantum wells such as InAs/GaSb quantum wells where high efficiency sub-bandgap (i.e., photon energy below the bandgap of GaSb)[1] photon absorption occurs. In homojunction band structure engineering, such type-II quantum well can be best approximated by an abrupt p-n junction with strictly confined space in the junction axis. The abrupt p-n junction separates the electrons and holes on either side of the thin (e.g., 20-40 nm) depletion

region while the strong spatial confinement form both ends of the p-n junction defines the width of the quasi-quantum well. Fig. 2.1 shows the comparisons between a type-II InAs/GaSb quantum well and a confined Si p-n junction.

To enable the sub-bandgap light absorption, Franz–Keldysh effect is applied as shown in Fig. 2.2. However, the much larger dimensions of the Si structure than the type-II quantum well reduce the coupling between electrons and holes on either side of the p-n junction, causing the significant decrease in the sub-bandgap light absorption. The indirect bandgap of Si due to the k-selection rule imposed upon the light matter interaction which makes the situation even worse. To counter the above two constrains, the transition between energetic carrier states and bound impurity states has been used[2]. Since the impurity state is highly localized, optical transition involving an impurity state has a greatly relaxed k-selection rule due to the larger uncertainty of the k-vector of impurity state as illustrated in Fig. 2.3.

On the other hand, energetic carrier states well above the bottom of the conduction band produce a strong penetration depth (i.e., wave function spillover) to reach the opposite side of the p-n junction to facilitate electron-impurity state coupling, as shown in Fig. 2.1. For such energetic carriers, the effective barrier width is significantly lower than the physical width of depletion region. Under a given optical wavelength, the “effective” barrier width experienced by the energetic carriers is further reduced with increasing reverse bias. Finally, near the top of the potential barrier, the axial velocity of the electron slows down, similar to a pendulum coming to a stop where its kinetic energy is converted into potential energy. This

effectively increases the probability of the energetic electron near the impurity state, thus further increasing the optical absorption coefficient.

To summarize, by forming a heavily doped, abrupt p-n junction with strong space confinement in the junction axis and by utilizing the optical excitation involving impurity-states and energetic carrier states, we expect to achieve high 1310 nm wavelength absorption in Si without relying on material defects or surface states.

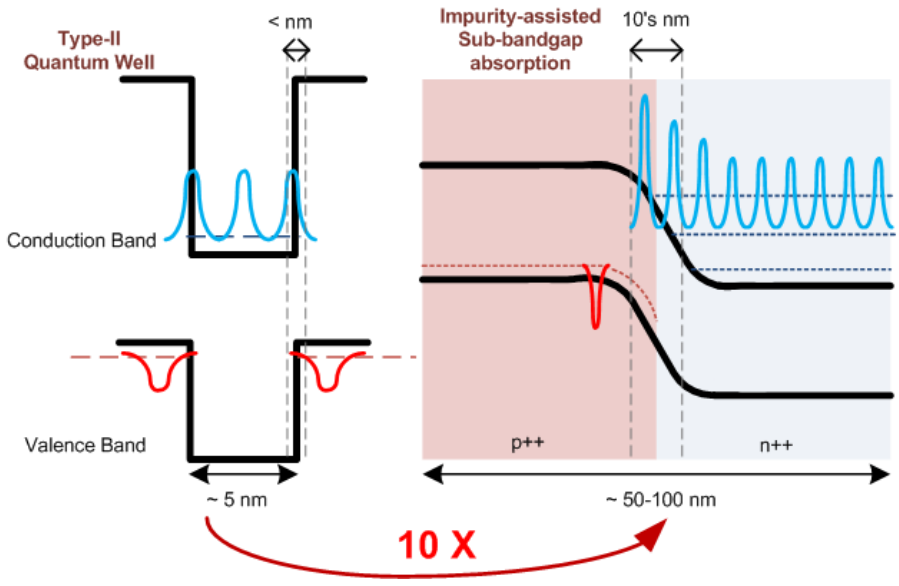

Figure 2.1: Device concept inspired by the type-II quantum wells. Comparisons between a InAs/GaSb quantum well and a confined Si p-n junction, which use transitions between energetic carrier states and bound impurity states.

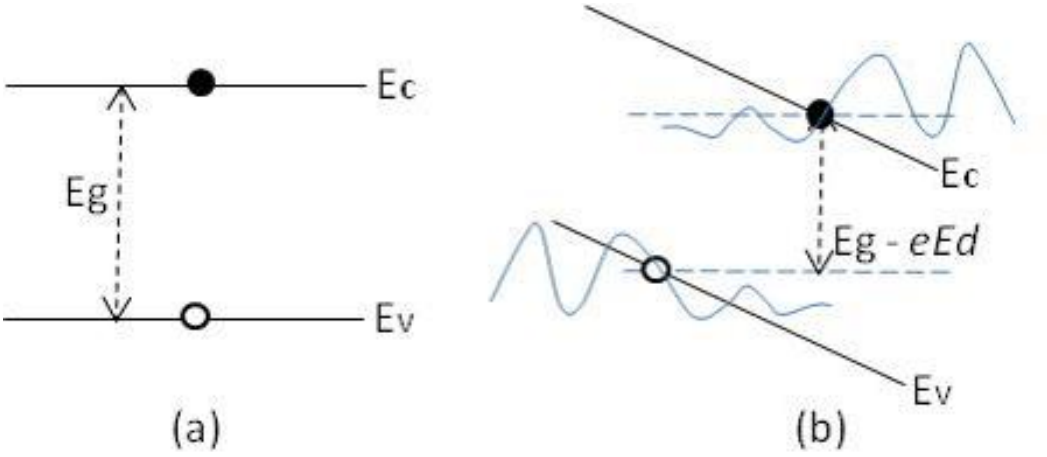

Figure 2.2: Illustration of how a (a) Conventional band-to-band transition by optical excitation, (b) Real-space indirect transition by sub-bandgap photon absorption due to Franz-Keldysh effect.

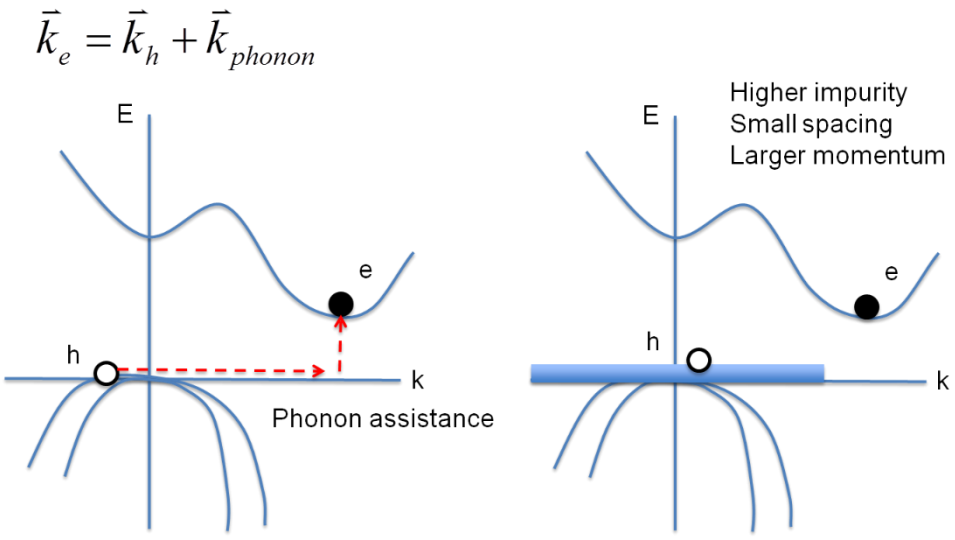

Figure 2.3: Illustration of k-selection rule relaxation. When the hole in the impurity band has a localized wave function (non-Bloch wave) without a well-defined crystal momentum. Hence the e-h excitation does not require satisfaction of the k-selection rule.

2.3 Experimental Results

The device on the SOI (silicon on insulator)substrate has a SiN lead waveguide that butt-couples the light to the Si detector. The Si detector has a short section of 1.5 µm wide waveguide leading to a 15 µm radius disk or ring that supports whisper gallery modes as shown in Fig. 2.4. Both the disk and ring structures produce nearly identical optical characteristics, and the devices results from the disk structure will be presented in the following sessions because it gives lower series resistance and a more precise reading on the actual bias voltage over the p-n junction.

2.3.1 Device Fabrication

The Si homojunction structure has been grew by OMCVD on a SOI substrate having 160 nm thick lightly doped p-Si layer on a 400 nm thick embedded oxide layer. The epitaxial layers, from the SOI side up, consist of 40 nm p-Si (6×10^{18} cm^{-3}), 5 nm n-Si (6×10^{18} cm^{-3}), 125 nm n-Si (2×10^{17} cm^{-3}), and 20 nm n-Si (3×10^{18} cm^{-3}). The micrograph of the fabricated device is shown in Fig. 2.4 (c). The Si epitaxial layers on the SOI wafer were photolithography patterned and etched to form the Si waveguide and the ring/disk resonator with one n-contact on the top surface flanked by to p-contacts. The p-contacts were formed by precisely removing the top 150 nm thick n-layers using dry etch. The lead SiN waveguide that connects the external light source and the detector was deposited and patterned on the 400 nm SiO_2 of the SOI wafer after removing all the Si epitaxial layers over than SiN regime. The SiN layer was designed to have the same thickness (350 nm) of Si layers to facilitate the

light coupling. The SiN waveguide and the waveguide section of the Si detector were formed in a self-aligned process as shown in Fig. 2.5.

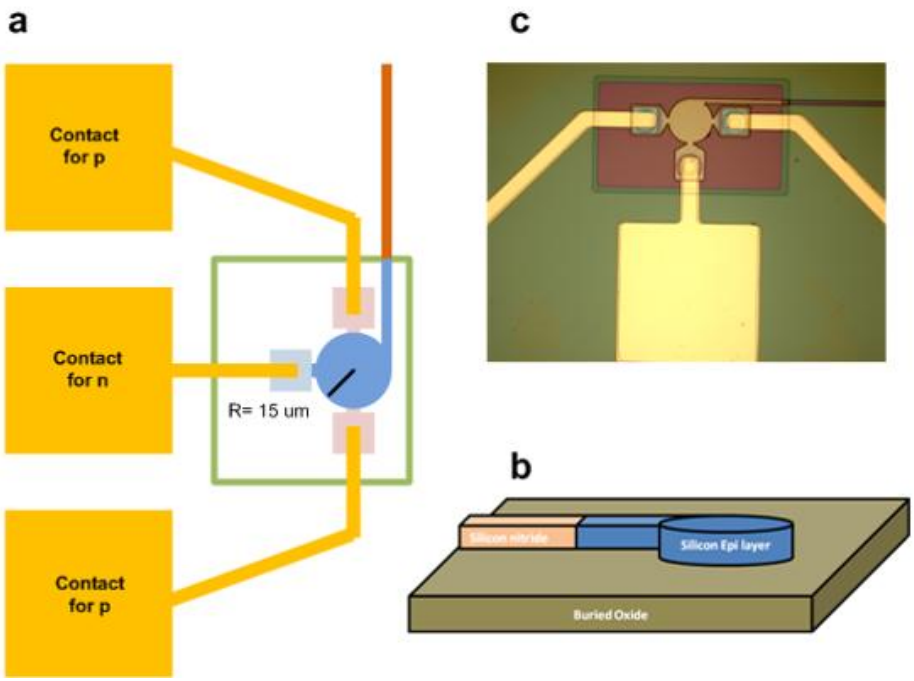

Figure 2.4: A schematic of the device. a, Top view and b, the cross-section of the disk device. c, Homojunction band structure engineering uses only the device geometry, doping profile, and regular dopants used in Si process to tailor the optoelectronic properties of the device.

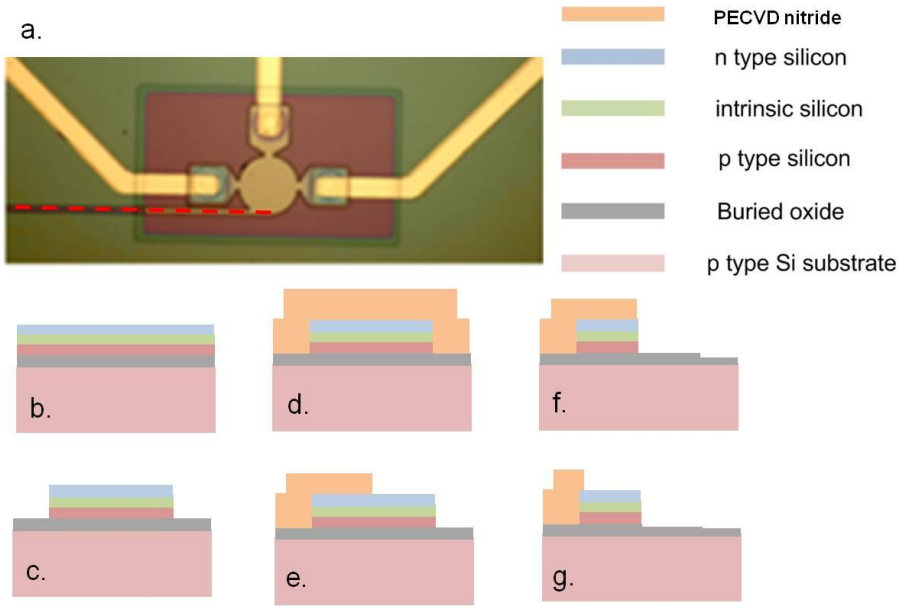

Figure 2.5: Self-alignment process of the silicon and SiN_x waveguide. The fabrication process for the cross-section of the red dash line region in a. is illustrated in b. to g.

2.3.2 Internal quantum efficiency Measurement

The internal quantum efficiency (QE) values were extracted from two measurement data for long waveguide and disk structures. The measurement setup is illustrated in Fig. 2.6. The ratio of the internal quantum efficiency of two wavelengths is,

$$\frac{I_{1310}(L,V)}{I_{635}(L,V)} = \left(\frac{P_{1310}}{P_{635}}\right)\left(\frac{\lambda_{1310}}{\lambda_{635}}\right)\left(\frac{\eta_{1310}}{\eta_{635}}\right)\frac{QE_{1310}(L,V)}{QE_{635}} \cong \left(\frac{P_{1310}}{P_{635}}\right)\left(\frac{\lambda_{1310}}{\lambda_{635}}\right)\left(\frac{\eta_{1310}}{\eta_{635}}\right)QE_{1310}(L,V) \quad (2.1)$$

Where $I_{1310}(L,V)$ and $I_{635}(L,V)$ is the measured photocurrent at wavelength 1310 nm and 635 nm, P_{1310} and P_{635} is the input light power for the 1310 nm and 635 nm, λ is the wavelength of two different laser, η is the coupling efficiency of the fiber butt coupling for two different laser. Since during the same device measurement, the fiber was not moved, η is the same in the same device measurement.

I first measured the photocurrents on a long waveguide device with two different laser lights. Assuming that the light can be absorbed completely by mm-long waveguide structure for both 635 nm and 1310 nm wavelengths, the ratio from Eq. (2.1) can be written as,

$$\frac{I_{1310}(\infty,V)}{I_{635}(\infty,V)} = \left(\frac{P_{1310}}{P_{635}}\right)\left(\frac{\lambda_{1310}}{\lambda_{635}}\right)\left(\frac{\eta_{1310}}{\eta_{635}}\right) \quad (2.2)$$

Secondly, I measured the photocurrent on the target disk device with two different wavelength light, the ratio can be represented as,

$$\frac{I_{1310}(L,V)}{I_{635}(L,V)} = \frac{I_{1310}(\infty,V)}{I_{635}(\infty,V)}\,QE_{1310}(L,V) \quad (2.3)$$

The internal QE can be extracted from Eq.(2.2) and Eq.(2.3). The different bias dependence of the detector response to 635 nm and 1310 nm light is observed as Fig. 2.7. This manifests the fundamentally different absorption mechanism for the Si structure to photons above and below the energy bandgap.

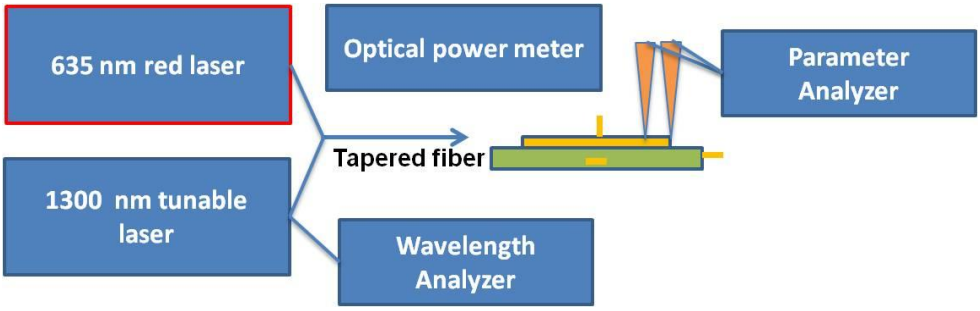

Figure 2.6: Quantum efficiency measurement system.

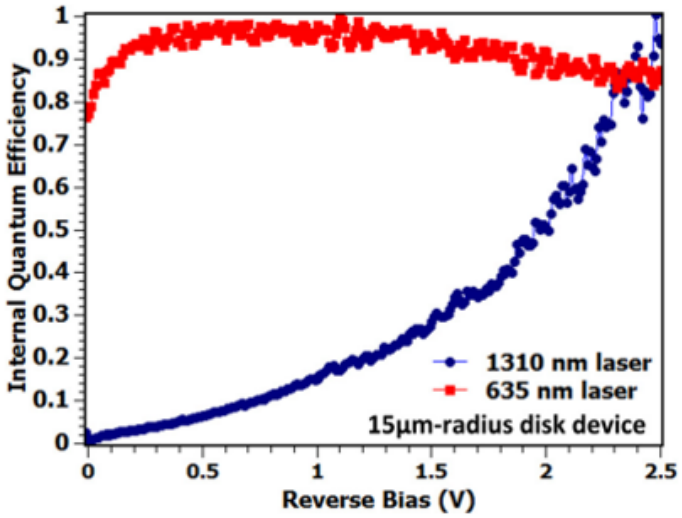

Figure 2.7: Internal quantum efficiency of 635 nm and 1310 nm light.

2.3.3 Spectral Response

The spectral response was measured with the same system and the Thorlabs 1300 nm tunable laser (TLK-L1300R). The photocurrent across 1280 nm to 1360 nm wavelength range at -1V was measured and the internal QE can be obtained by the same method I mentioned in 2.3.2. In addition, the spectral internal QE can be extracted from Fig. 2.8. Due to the effect of resonant cavities compounded with multi-mode (polarization) interference, the device shows wavelength dependent internal QE. At 2.5 V reverse bias, the internal QE near the resonant wavelength reaches nearly 100% (with 5% error of measurement).

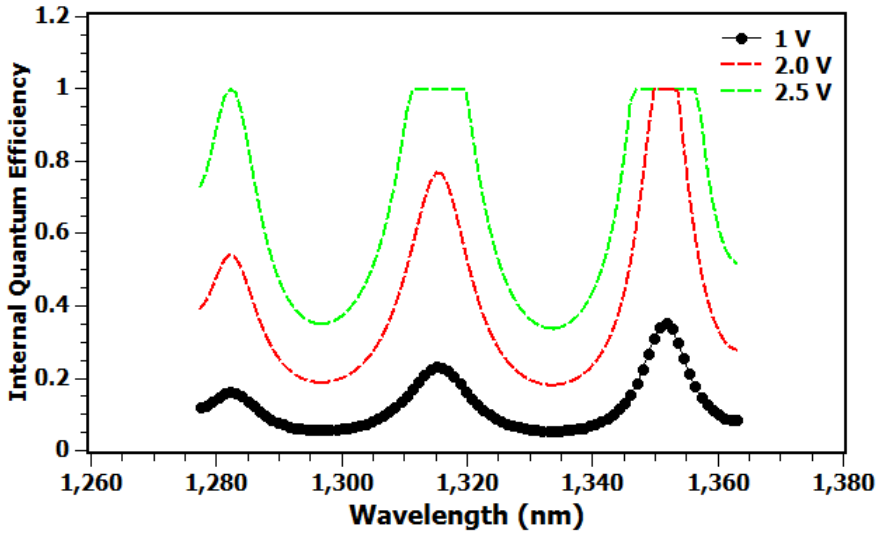

Figure 2.8: Spectrum response of the device. The wavelength dependence responsivity of the disk device at -1V was measured. Also for the wavelength dependent quantum efficiency at -2 V and -2.5 V can be acquired based on the trend of the data at -1V and the values of -2 V and -2.5 V in Fig. 2.7.

2.4 Conclusion

By forming a heavily doped, abrupt p-n junction with strong space confinement in the junction axis, and by utilizing the optical excitation involving impurity-states and energetic carrier states, a waveguide coupled disk device with absorption coefficient around 10 cm^{-1} in Si without relying on material defects or surface states is demonstrated. The spectral response also shows high internal quantum efficiency near 100% in 1300 nm wavelength regime.

Portions of this chapter have been published in Applied Physics Letter 2013 by Yu-Hsin Liu, Yuchun Zhou, and Yu-Hwa Lo. The dissertation author was the primary investigator and author of this paper.

Chapter 3 Quantum Mechanics Calculations for Light Absorption Coefficient in Silicon

3.1 Overview

From the Fermi Golden Rule and the time-dependent perturbation theory[1-2], the absorption coefficient for an indirect bandgap semiconductor that is heavily doped to produce an impurity band can be simply written as,

$$\alpha(E_{cv}) = \left\{ \sum_c \sum_{vi} \frac{2\pi}{\hbar} \left| \langle \psi_e^*(r,t) H \psi_{vi}(r,t) \rangle \right|^2 (f_v - f_c) + \sum_{ci} \sum_v \frac{2\pi}{\hbar} \left| \langle \psi_{ei}^*(r,t) H \psi_h(r,t) \rangle \right|^2 (f_v - f_c) \right\} / \left(\frac{I}{\hbar\omega} \right)$$

(3.1)

In (3.1), $\psi_e^*(r,t)$ and $\psi_h(r,t)$ are the wave functions of electrons and holes in the conduction and valance bands. ψ_{ei}^* and ψ_{vi} are the wave functions of electrons and holes in the impurity states. H is the interaction Hamiltonian. For indirect bandgap semiconductor such as silicon, absorption of subbandgap photons by electrons and holes in the conduction and valence bands has little contribution due to the constraint of k-selection rule. Therefore, this term is neglected in (3.1). The Fermi functions f_c and f_v represent the probability for a state to be occupied by an electron or hole, and I is the optical power intensity upon the device.

In the following, we describe how we calculate subbandgap light absorption due to quasi 2D electron states and spatially confined acceptor states. All the electron states contributing to absorption of subbandgap energy photons need to satisfy the following condition required by the law of energy conservation:

$$\hbar\omega + \varepsilon + e\left|\phi_{bi}(x_0) + V(x_0)\right| \geq E_{e,no} + E_g \tag{3.2}$$

Here $\hbar\omega$ is the energy of the incident photons, ε is the ionization energy of acceptor, assumed to be 45 meV[3] above the valence band edge for boron, $e\left|\phi_{bi}(x_0) + V(x_0)\right|$ is the sum of the built-in potential and the applied reverse bias voltage at position x_0, $E_{e,no}$ is the electron energy of each subband in a confined p/n junction, and E_g is the bandgap energy. The relations among different energies in (3.2) are shown schematically in Fig. 3.1. The details derivation will be illustrated in the following sessions.

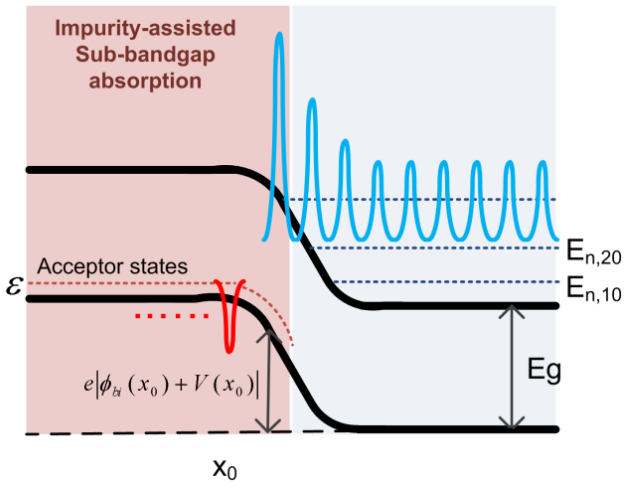

Figure 3.1: Absorption due to all available quasi 2D electron states and acceptor states.

3.2 Calculation for Matrix Element

Now we illustrate how to deal with the integration between the wave functions of electron and hole. The matrix element enters the expression of the absorption or stimulated emission as Eq. (3.3).

$$\left|M_{if}\right|^2 = \hbar^2 \left|\int_V \varphi_e^* \frac{\partial}{\partial x} \varphi_h^* dxdydz\right|^2 \tag{3.3}$$

Since the magnitude of the k-vector for photons is typically much smaller than the magnitude of k-vectors for electrons and holes with energies about 1-2 *k*T above the band edge where the density of states has a significant value, we have ignored the k for photons in the following treatment. For simplicity, we have also assumed that the light wave is linearly polarized in the x-axis.

According to our intuitive arguments that the highest sub-bandgap absorption for Si nanostructures relies on the combination of Franz-Keldysh effect, quantum confinement, and impurity state absorption, the most important contribution to sub-bandgap absorption occurs between an impurity (bound) state and a quasi-2D state. In other words, absorption of a sub-bandgap photon could excite a quasi-2D electron and a hole in the acceptor state or excite a quasi-2D hole and an electron in the donor state. The treatments of these two conditions are similar, so here we derive the expression of the matrix element due to one process: a quasi-2D electron state and an acceptor state in the impurity band extended from the valence band.

Now we consider the fact that for indirect bandgap semiconductor such as Si, the wavefunction of nth quantized state can be written as

$$\varphi_e^* = \frac{e^{i(k_{e\perp}-k_{o\perp})r_\perp} u_c(r)\xi_{e,n}(x)}{\sqrt{V}} \tag{3.4-a}$$

where $k_{o\perp}$ represents the k-vector at the conduction band minimum normal to the x-axis. For Si, there are 4 conduction band minimum satisfying this condition.

$$\varphi_e^* = \frac{e^{i(k_{e\perp})r_\perp} u_c(r)\xi_{e,n}(x)e^{-ik_{xo}x}}{\sqrt{V}} \tag{3.4-b}$$

where k_{xo} represents the k-vector at the conduction band minimum in parallel with the x-axis. For Si, there are 2 conduction band minimum satisfying this condition. $\xi_{e,n}(x)$ is the envelope function for electrons in the nth sub-band.

The localized acceptor state wave function can be approximated as,

$$\varphi_h^* = \eta(r, x_o)u_v(r) \tag{3.5}$$

where $u_h(r)$ is the usual atomic wave function and $\eta(r, x_0)$ represents the spatial distribution of an impurity state at location x_0. Since $u_v(r)$ are periodic functions with the lattice constant as the period, they can be represented as,

$$u_c(r) = \sum_G a_G e^{iGr} \qquad u_v(r) = \sum_{G'} b_{G'} e^{iG'r} \tag{3.6}$$

where G and G' are reciprocal lattice vectors. Also, we can represent the position vector, r, as the sum of a lattice vector and a position vector within one unit cell,

$$r = \rho_{h,k,l} + \gamma$$

where (h,k,l) are the indices for the position of the unit cell. Considering the fast-varying part: $u_c^* u_v$ is orthogonal so the integration with each unit cell is zero. Within

the unit cell, the slow varying part: $(e^{i(k_{o\perp})r_\perp} or\ e^{+ik_{ox}x})\xi^*_{e,n}(x)\frac{\partial\eta(r,x_o)}{\partial x}$ is basically a constant, hence Eq. (3.3) can be rewritten as,

$$\left|M_{if}\right|^2 =$$

$$\frac{\hbar^2}{V}\left|\sum_{G,G'} a^*_G b_{G'} G'_x \int_V\ e^{i(G'-G)r} e^{-ik_{e\perp}r_\perp}\ (e^{i(k_{o\perp})r_\perp} or\ e^{+ik_{ox}x})\xi^*_{e,n}(x)\eta(r,x_o)dxdydz + \right.$$

$$\left.\int_V\ u^*_c u_v e^{-ik_{e\perp}r_\perp}\ (e^{i(k_{o\perp})r_\perp} or\ e^{+ik_{ox}x})\xi^*_{e,n}(x)\frac{\partial\eta(r,x_o)}{\partial x}dxdydz\right|^2 \cong$$

$$\frac{\hbar^2}{V}\left|\sum_{G,G'} a^*_G b_{G'} G'_x \int_V\ e^{i(G'-G)r} e^{-ik_{e\perp}r_\perp}\ (e^{i(k_{o\perp})r_\perp} or\ e^{+ik_{ox}x})\xi^*_{e,n}(x)\eta(r,x_o)dxdydz\right|^2$$

(3.7)

Again (3.7) can be further reduced to (3.8)

$$\left|M_{if\ \ 4-fold}\right|^2 \cong \frac{|M_b|^2}{V}\left|\int_{(y-z\ plane)} e^{-i(k_{e\perp}-k_{o\perp})r_\perp}\left[\int_0^L \xi^*_{e,n}(x)\eta(r,x_o)dx\right]dydz\right|^2$$

(3.8-a)

$$\left|M_{if\ \ 2-fold}\right|^2 \cong \frac{|M_b|^2}{V}\left|\int_{(y-z\ plane)} e^{-i(k_{e\perp})r_\perp}\left[\int_0^L \xi^*_{e,n}(x)\eta(r,x_o)\ \ e^{+ik_{ox}x}dx\right]dydz\right|^2$$

(3.8-b)

Define functions $G'_n(y,z,x_o)$ and $G''_n(y,z,x_o)$, both have unit $L/\sqrt{V}$, for an impurity state at position x_o

$$G'_n(y,z,x_o) = \left[\int_0^L \xi^*_{e,n}(x)\eta(r,x_o)dx\right]$$

(3.9-a)

$$G''_n(y,z,x_o) = \left[\int_0^L \xi^*_{e,n}(x)\eta(r,x_o)\ \ e^{+ik_{ox}x}dx\right]$$

(3.9-b)

Define functions $\mathcal{G}'_n(k_{e\perp}, x_o)$ and $\mathcal{G}''_n(k_{e\perp}, x_o)$, both have unit $\sqrt{V}$,

$$\mathcal{G}'_n(k_{e\perp}, x_o) = \int_{(y-z\ plane)} e^{-i(k_{e\perp}-k_{o\perp})r_\perp} G'_n(y, z, x_o)\, dydz \quad (3.10\text{-a})$$

$$\mathcal{G}''_n(k_{e\perp}, x_o) = \int_{(y-z\ plane)} e^{-i(k_{e\perp})r_\perp} G''_n(y, z, x_o)\, dydz \quad (3.10\text{-b})$$

$\mathcal{G}'(k_{e\perp}, x_o)$ is the 2D Fourier transform of $G'(y, z, x_o)$. $\mathcal{G}''(k_{e\perp}, x_o)$ is the 2D Fourier transform of $G''(y, z, x_o)$.

The matrix element between an electron and a bound acceptor state at position x_o can be written as

$$\left|M_{if\ \ 4-fold}\right|^2 = \frac{|M_b|^2}{V} |\mathcal{G}'_n(k_{e\perp}, x_o)|^2 \quad \text{for the n}^{\text{th}} \text{ quantization state}$$

(3.11-a)

$$\left|M_{if\ \ 2-fold}\right|^2 = \frac{|M_b|^2}{V} |\mathcal{G}''_n(k_{e\perp}, x_o)|^2 \quad \text{for the n}^{\text{th}} \text{ quantization state}$$

(3.11-b)

3.3 Calculations of the absorption coefficient: α(E)

The absorption coefficient is the ***sum*** of the absorption coefficient between each pair of states in the conduction band and valence band. It can be written as

$$\alpha(E) = \frac{e^2 h}{2\epsilon_o m_o^2 c\bar{n}E} \frac{1}{V} \iint_{k_e, k_h} \left|M_{if}\right|^2 \delta(E_e + E_h - E)(1 - f_c - f_v) \frac{2V}{(2\pi)^3} d^3k_e \frac{V}{(2\pi)^3} d^3k_h \quad (3.12)$$

Note that Eq. (3.12) is the "net absorption" which is equal to the absorption minus emission. The "net absorption" has the Fermi function term: $(1 - f_c)(1 - f_v) - f_c f_v = 1 - f_c - f_v$. Also note that the Fermi function for holes f_v is defined as

the "probability for a state to be occupied by a hole". This definition treats holes in the same way as electrons except that the "hole energy" is "pointing downward" (i.e. hole energy at the top of the valence band is zero and holes deeper in the valence band has a higher positive energy). In consistency with this definition, we use $\delta(E_e + E_h - E)$ in the Fermi Golden rule instead of the typical expression $\delta(E_e - E_h - E)$ in most textbook. In those textbooks, the term $(1 - f_c - f_v)$ should be written as $f_v - f_c$.

Also note that we only multiple the spin-degeneracy (x2) once because the light absorption has to satisfy the conservation of spin angular momentum since linearly polarized photons contain no spin. In other words, once the spin state of one carrier (e.g. electron) is determined, the spin of the other carrier is also determined.

Here, we only discuss the absorption coefficient between quasi-2D electrons and holes in impurity (or defect) states. Assume there are multiple impurity (acceptor) states each having a concentration profile $P_m(x)$ and an ionization energy ε_m. The absorption coefficient due to all available quasi 2D electron states for 4-fold and acceptor states can be represented as

$$\alpha_{4-fold}(E) = \frac{e^2 h|M_b|^2}{2\epsilon_o m_o^2 c\bar{n}E}\frac{1}{V^2}\sum_n\sum_m A\int_{x_o=0}^{L}\rho_{h,m}(E_h)dx_o$$
$$\iint_{k_{e,\perp}-k_{o\perp},E_h}\left|\mathcal{G}'_n(k_{e\perp},x_o)\right|^2\delta(E_e+E_h-E)(1-f_c-f_v)\frac{2A}{(2\pi)^2}d^2\left(k_{e,\perp}-k_{o\perp}\right)dE_h \quad (3.13\text{-a})$$

$$\alpha_{2-fold}(E) = \frac{e^2 h|M_b|^2}{2\epsilon_o m_o^2 c\bar{n}E}\frac{1}{V^2}\sum_n\sum_m A\int_{x_o=0}^{L}\rho_{h,m}(E_h)dx_o$$

$$\iint_{k_{e,\perp},E_h}|\mathcal{G}''_n(k_{e\perp},x_o)|^2\delta(E_e+E_h-E)(1-f_c-f_v)\frac{2A}{(2\pi)^2}d^2\left(k_{e,\perp}\right)dE_h$$

(3.13-b)

To obtain (3.13), note that $\mathcal{G}'_n(k_{e\perp},x_o)$, and $\mathcal{G}''_n(k_{e\perp},x_o)$ are all position dependent since they represent the interaction between an electron state and a bound acceptor state at a given position. If the bound acceptor state is far from the p-n junction, then their values diminish quickly.

$$\rho_{h,m}(E_h) = P_m(x)\delta(E-E_h+E_n) \tag{3.14}$$

The density of acceptor state is zero except when $E_h = -\varepsilon_m$, the ionization energy of the acceptor state.

If $\mathcal{G}'_n(k_{e\perp})$ and $\mathcal{G}''_n(k_{e\perp})$ depend only on the magnitude but not on the direction of $k_{e\perp}$, then $d^2k_{e,\perp}$ can be written as $2\pi k_{e,\perp}dk_{e,\perp}$. Using effective mass approximation for electrons:

For type-II quantum wells and consider the 4-fold/2-fold degeneracy of the conduction band,

$$E_{e,n,4-fold} = E_g - e\left|\phi_{bi}+V\right| + E_{e,no} + \frac{\hbar^2(k_{e\perp}^2-k_{o\perp}^2)}{2m_e} \tag{3.15-a}$$

$$E_{e,n,2-fold} = E_g - e\left|\phi_{bi}+V\right| + E_{e,no} + \frac{\hbar^2(k_{e\perp}^2)}{2m_e} \tag{3.15-b}$$

The delta functions in Eq. (3.14) can be revised as,

$$\delta(E_e+E_h-E) = \delta\left(E_h-(E+e\left|\phi_{bi}+V\right|-E_g-E_{e,no}-\frac{\hbar^2(k_{e\perp}^2-k_{o\perp}^2)}{2m_e})\right) \tag{3.16-a}$$

for 4-fold degeneracy of the conduction band,

$$\delta(E_e + E_h - E) = \delta\left(E_h - (E + e|\phi_{bi} + V| - E_g - E_{e,no} - \frac{\hbar^2 k_{e\perp}^2}{2m_e})\right) \qquad (3.16\text{-b})$$

for 2-fold degeneracy of the conduction band,

Substituting (3.16) into (3.13) and using the properties of δ-function, we have

$$\alpha_{4-fold}(E) = \frac{e^2 h|M_b|^2}{2\epsilon_o m_o^2 c\bar{n}E}\frac{1}{V^2}\sum_n\sum_m A\int_{x_o=0}^{L} dx_o \int_{k_{e,\perp}-k_{o\perp}} |\mathcal{G}'_n(k_{e\perp})|^2 (1 - f_c - f_v)P_m(x_o)\delta(\varepsilon_m + E + e\phi bi + V - Eg - Ee,no - \hbar 2(ke\perp 2 - ko\perp 2)2me)2A2\pi 2d2ke,\perp - ko\perp$$

(3.17-a)

$$\alpha_{2-fold}(E) = \frac{e^2 h|M_b|^2}{2\epsilon_o m_o^2 c\bar{n}E}\frac{1}{V^2}\sum_n\sum_m A\int_{x_o=0}^{L} dx_o \int_{k_{e,\perp}} |\mathcal{G}''_n(k_{e\perp})|^2 (1 - f_c - f_v)P_m(x_o)\delta(\varepsilon_m + E + e\phi bi + V - Eg - Ee,no - \hbar 2(ke\perp 2 - ko\perp 2)2me)2A2\pi 2d2ke,\perp$$

(3.17-b)

Equation (3.17) shows the absorption coefficient when a quasi-2D electron and a hole in the acceptor state are created. The quasi-2D electron is in the n-side and the hole in the acceptor state is in the p-side of the Si p/n junction.

3.4 Practical Calculation Details

The localized acceptor state wave function can be approximated as $\psi_h = \eta(r, x_0)u_h(r)$, where $u_h(r)$ is the usual atomic wave function and $\eta(r, x_0)$ represents the spatial distribution of an impurity state at location x_0. For simplicity, we approximate $\eta(x, y, z, x_0) = (1/(2a^*)^{3/2})$ if $|x - x_0| \le a^*, |y| \le a^*, |z| \le a^*$, and $\eta(x, y, z, x_0) = 0$ elsewhere, with a^* being the Bohr radius calculated from the equation $a^* = (4\pi\varepsilon\hbar^2 / m_h^* e^2)$.

By substituting these wave functions into (3.17), we can obtain the expressions of absorption coefficient from the 4-fold and 2-fold degeneracy states of quasi 2D electrons:

$$\alpha_{4-fold}(E) \cong \mathrm{M}_{4\text{-fold}} \sum_{x_0} \left[P(x_0)^{-1/3}\right] \left[\sum_n \left|\xi^*_{e,n}(x_0)\right|^2\right] (f_v - f_c) P(x_0) \frac{\sin^4\left[k_{e\perp} a^*\right]}{\left[k_{e\perp} a^*\right]^4} \frac{2\pi m_e}{\hbar^2} \quad (3.18\text{-a})$$

where $\mathrm{M}_{4\text{-fold}} = \dfrac{e^2 h \left|M_b\right|^2}{2\varepsilon_0 m_0^2 c \bar{n} E} \dfrac{1}{V} \dfrac{1}{L} (2a^*)^3 \dfrac{2A}{(2\pi)^2}$

$$\alpha_{2-fold}(E) \cong M_{2-fold} \left|\frac{2\sin(k_{0x} a^*)}{k_0 (2a^*)^{3/2}}\right|^2 \sum_{x_0} \left[P(x_0)^{-1/3}\right] \sum_n \left|\xi^*_{e,n}(x_0)\right|^2 (f_v - f_c) P(x_0) \frac{\sin^4\left[k_{e\perp} a^*\right]}{\left[k_{e\perp} a^*\right]^4} \frac{2\pi m_e}{\hbar^2} \quad (3.18\text{-b})$$

where $M_{2-fold} = \dfrac{e^2 h \left|M_b\right|^2}{2\varepsilon_0 m_0^2 c \bar{n} E} \dfrac{1}{V} \dfrac{1}{L} (2a^*)^4 \dfrac{2A}{(2\pi)^2}$

In Eqs. (3.18-a) and (3.18-b), L is the thickness of the epitaxial silicon p-n junction, and A and V are the area (y-z plane) and volume of the device. The value of $\left|M_b\right|^2$ can be determined approximately by $\left|M_b\right|^2 = 1.33 m_0 E_g$ in a quasi-quantum confined system[4]. $P(x_0)$ is the doping concentration profile of acceptor and $k_\perp = (2m_e^* \Delta E)^{1/2} / \hbar$, where ΔE is the kinetic energy of an electron in a specific sub-band. Electron wave function at each position $\xi^*_{e,n}(x_0)$ is extracted from the simulation results of software, Silvaco, as shown in Fig. 3.2.

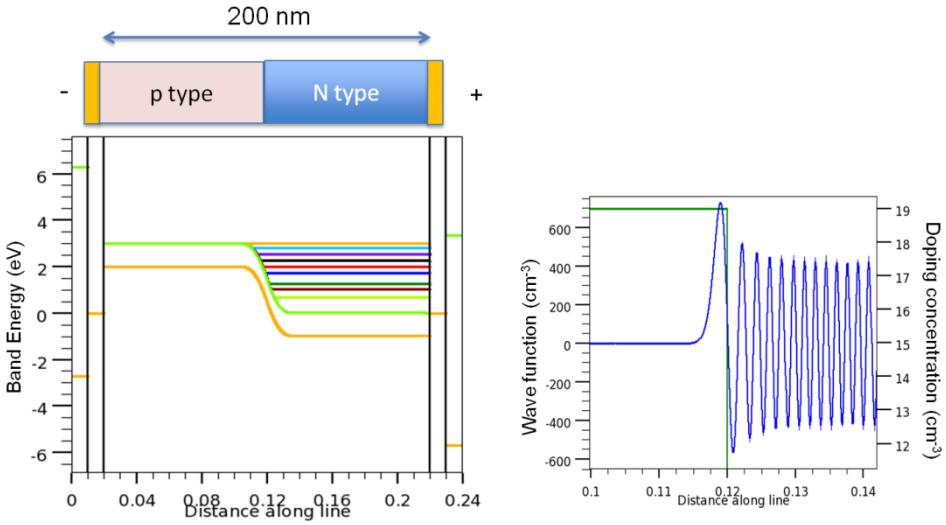

Figure 3.2: Simulated results of Silvaco, Left: p-n junction structure with energy states in the conduction band, Right: wave function of one picked energy state.

3.5 Calculation Results

With Eq. (3.18), and the simulated results from Silvaco, the sub-bandgap absorption coefficient can be calculated as shown in Fig. 3.3 and Fig. 3.4. The p-n junction structure, with 100 nm thick of each type, is established in Silvaco simulation and under different bias and different doping concentration conditions. The wavefunctions are obtained at each enerygy state in the conduction band.

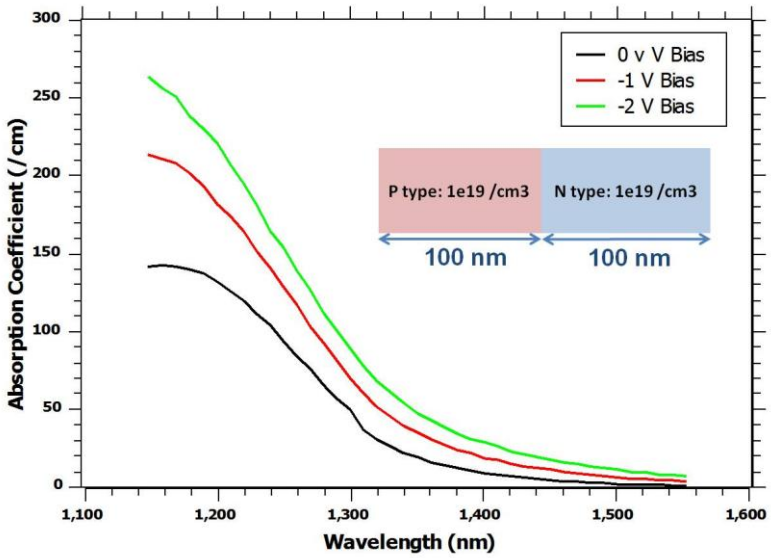

Figure 3.3: Bias dependence absorption coefficient.

The absorption coefficient increasing with the reverse bias application because Franz-Keldysh effect is more effective at higher bias, and the absorption coefficient decreases with the increasing wavelength because the incident photon energy is smaller at larger wavelength. The higher doping concentration case also shows higher absorption coeeficient since it helps relax the k-selectrion rule.

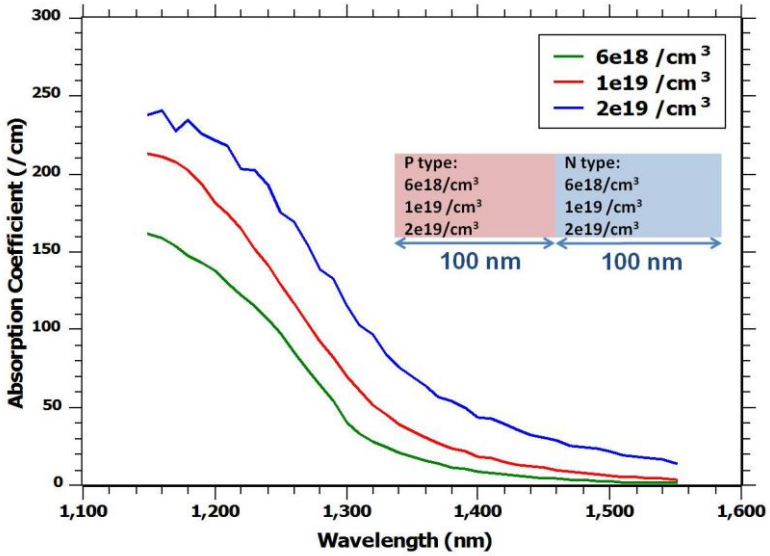

Figure 3.4: Doping concentration Dependence absorption coefficient.

The device strcture mentioned in the last chapter is also simulated in Silvaco and the theorytical absorption coefficient is calculated in Fig. 3.5.b. Compared with the measured absorption coefficinet result in Fig. 3.5.a, the theory and experiment show good agreements in their general characteristics. The differences in the numerical values could be due to the approximate wave function for impurity states, the aproximation of the impurity band into a single energy level, and the difference between the real and designed impurity profiles.

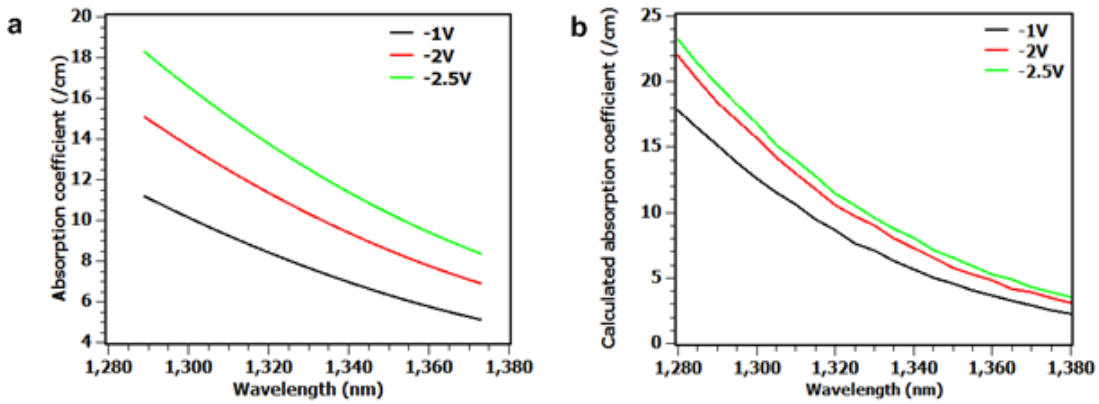

Figure 3.5: Wavelength dependent absorption coefficient. Wavelength dependent modal absorption under different bias voltage for (a) experimental results and (b) theoretical calculations.

3.6 Conclusion

The heavily doped p-n junction structure can be modeled by using first principle calculation and the simulation software to obtain the wave functions of the 2-D confined layer. The theory and experiment show good agreements in their general characteristics.

Portions of this chapter have been published in Applied Physics Letter 2013 by Yu-Hsin Liu, Yuchun Zhou, and Yu-Hwa Lo. The dissertation author was the primary investigator and author of this paper.

Chapter 4 Cycling Excitation Process

4.1 Overview

The cycling excitation effect comes from an optically excited carrier gaining sufficient energy across the junction to excite a new electron-hole pair which provides a carrier of the opposite charge to start another pair excitation. We hypothesize that the high efficiency of the cycling excitation process is due to the strong transitions of the localized states of the compensating impurities via Coulomb interactions with the energetic carriers. These localized states relax the k-selection rule (momentum conservation), thus enhancing the probability of new e-h pair generation via collision between the energetic carrier and localized electrons (holes).

4.2 Physical Mechanism

As an illustration, consider an electron accelerated by a potential drop in crossing the p-n junction towards the n-region (Fig.4.1(a)). In the heavily compensated n-region, the photo-generated electrons acquires sufficient energy for an Auger process to excite an electron across the band gap from the acceptor. The hole left behind is susceptible to being filled by a valence band electron via phonon absorption (Fig. 4.1(b)). The Auger process is more probable from the acceptor than from the valence band because of the former's localized wave function, thus providing an explanation of the high excitation efficiency. Furthermore, the band hole thus created, in crossing back the p-n junction, has probability of a similar

Auger excitation to produce an additional electron-hole pair from the compensating donors in the p-region (Fig. 4.1(c)-(d)). The cycling process produces a series of events with geometrically decreasing probabilities, enhancing the photocurrent beyond the single electron-hole pair created by the original photon.

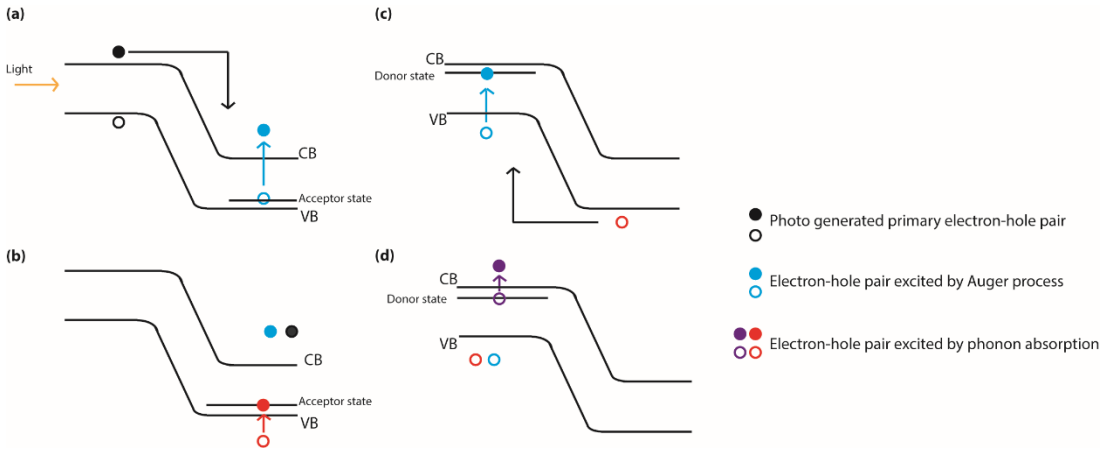

Figure 4.1: Illustration of the cycling excitation process.

4.3 Experimental Results

4.3.1 Device Fabrication

The compensated doped Si layers has been designed and fabricated to a device as shown in Fig 4.2. The device structure is grown by the organometallic chemical vapor deposition (OMCVD) technique to achieve precise control of the doping profile and layer thickness. The layer structure is the same as a conventional Si p-n junction device except that the layers near the junction have a high doping level and a doping concentration ratio (80%±5%).

The 650nm deep device mesa was formed by inductively coupled plasma reactive-ion etching (ICP-RIE) with C_4F_8 and SF_6 gases. The device mesa has a light sensitive area of 35 by 55 micrometers. After the mesa etch, a 300 nm thick layer of SiO_2 was deposited and patterned lithographically to form n- and p-metal contacts. E-beam evaporated Ti/Au was used to form the n- and p-Ohmic contacts. The metal contact was annealed at 290℃ for 40 seconds in a rapid thermal annealing chamber.

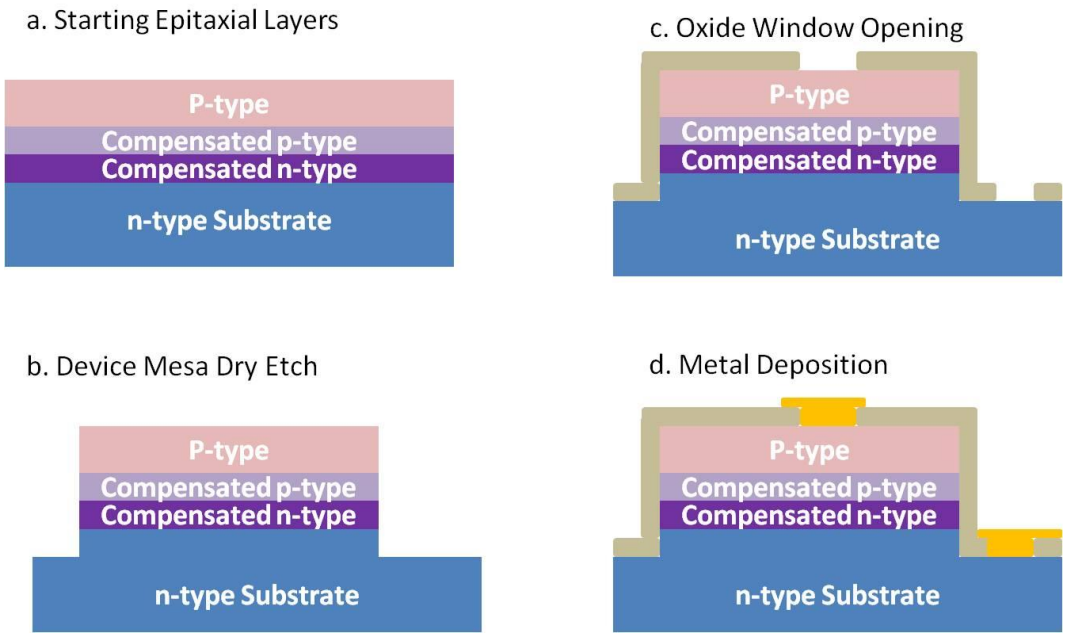

Figure 4.2: Device fabrication. (a) Starting Epitaxial Si substrate. (b) Device mesa etching. (c) Oxide window opening. (d) Metal Deposition for the contact.

4.3.2 Photoresponse measurement

Althgouh the device shows a rather typical p-n junction current-voltage characteristics in the dark condition, its photocurrent increases markedly with the reverse bias voltage, in sharp contrast with a standard p-n junction photodiode where the photoresponse remains nearly constant.

To measure the voltage and power dependence of photoresponse, the measurement setup is shown in Fig. 4.3(b). The 635 nm light illuminate the device by free space coupling. The device is under reverse bias and the light-off and light-on current values has been recorded from the Keithly source meter. The illumination light power is represented by the primary photocurrent at zero volt.

At a reverse bias voltage as low as 3V, the photoresponse gain reaches over 4000, as shown in Fig. 4.4. By contrast, for impact ionization to produce a gain of around 10, the p-n junction needs to be biased to over 20 V according to simulation (Silvaco software). Noteably, the gain of the CEP device decreases with increasing input optical power represented by the primary photocurrent as Fig.4.5.

When the input light power is increased, a large number of photo generated energetic carriers are able to trigger a lot of Auger excitations. However, since the phonon distribution and its dynamics, the localized phonon deficiency causes the incomplete CEP due to the limitation of the phonon absorption. This also happens at high reverse bias voltage regime, the saturation of the gain is shown in Fig. 4.4. When there’re more energetic carriers than the phonons, the multiplication gain is suppressed.

(a)

Compensated Layers	
Thickness (μm)	Doping(cm^{-3})
0.2	**$p=3\times10^{19}$ ($n=2$ to 2.5×10^{19})**
0.2	**$n=3\times10^{19}$ ($p=2$ to 2.5×10^{19})**

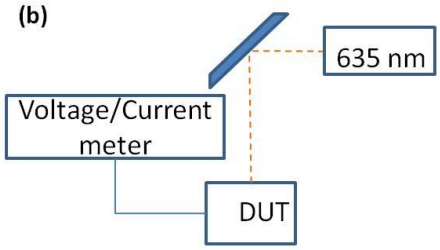

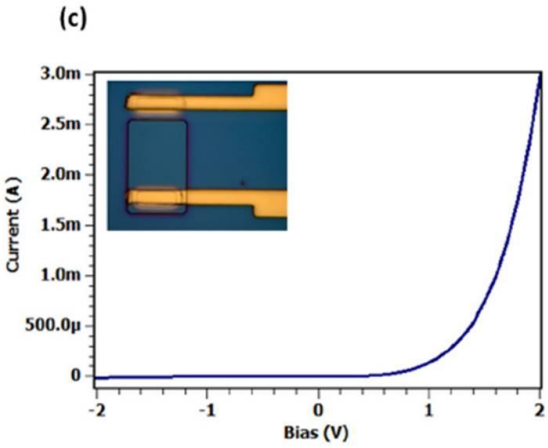

Figure 4.3: (a) Design of the partially compensated Si p-n junction. (b) Photoresponse measurement system with 635 nm laser and souce meter. (c) Dark I-V characteristics of the fabricated device. A typical p-n junction rectifying behavior was observed.

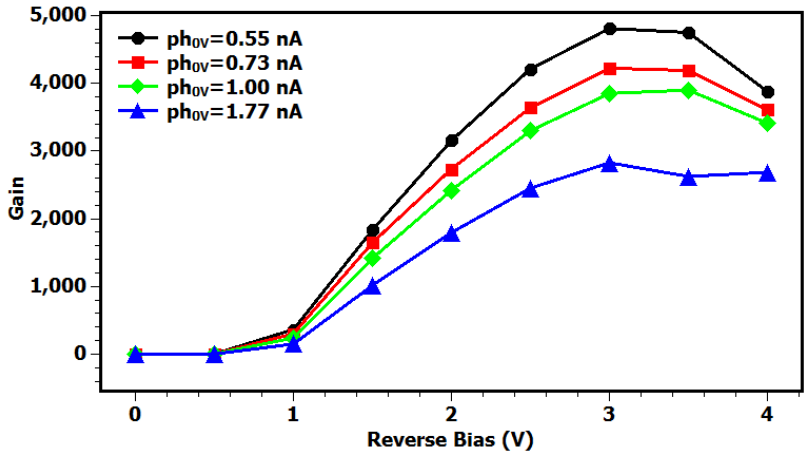

Figure 4.4: Bias dependence of gain. The illumination (635 nm) light power is represented by the primary photocurrent at zero volt.

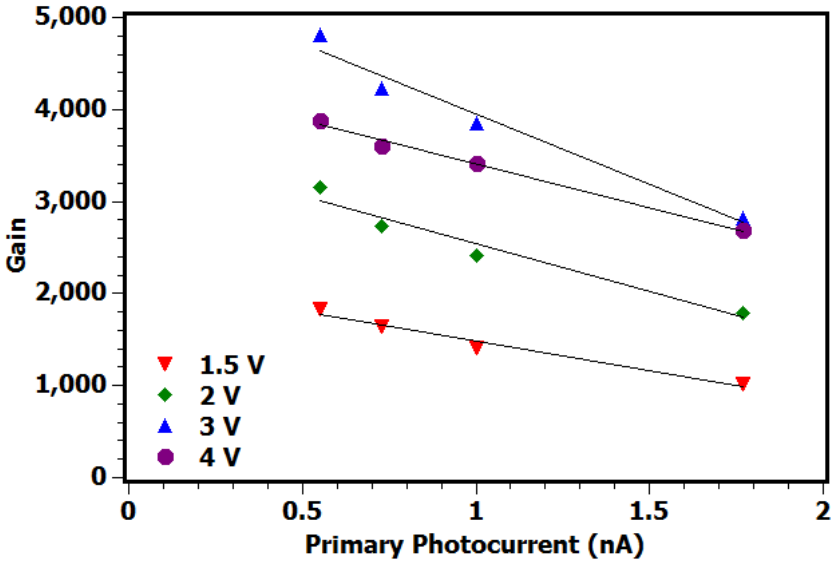

Figure 4.5: Input light intensity dependence of gain.

4.3.3 Temperature dependence measurement

The temperature dependence of response was performed on a packaged device in a cryochamber, which can be used for cooling control from liquid nitrogen temperature (~77K) to 400K. A temperature controller Lakeshore 325 was used to monitor and control the temperature inside the chamber. There're two thermal diodes, one is close to the actual packaged device to detect the actual temperature reading and another one was placed near the heater. The temperature dependence of gain shows a gain increase as the temperature increases from 140 K to 300K (Fig. 4.6). These results strongly suggest that phonons play significant roles in the CEP effect. The higher performance of the device with increasing temperature suggests that phonons actually assist in the amplification process rather than hinder it via phonon scattering.

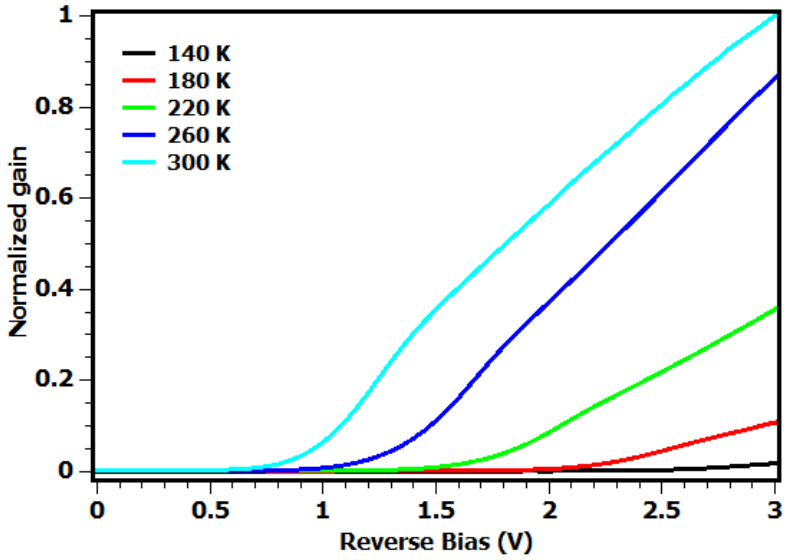

Figure 4.6: Temperature dependence of gain under 635 nm illumination in liner plot.

4.3.4 Excess Noise Factor measurement

Noise measurement was performed using the HP 8594E spectrum analyzer at 70MHz. An optical continuous-wave laser source at 635 nm was used to illuminate the device. The device was biased with a Keithley 2400 source meter through the inductor in the bias T and connected to the noise measurement system through the DC blocking capacitor in the bias T. Considering the high noise figure of the spectrum analyzer, a low noise amplifier (LNA) with a noise figure of 1.8dB was used to improve the system noise figure. The cascaded system noise figure was 2.76 dB, which yielded a system noise floor of -171 dBm/Hz. In order to provide impedance matching for LNA, a 50 Ω load was connected to the input of the LNA and the CEP device was connected with a parallel 50 Ω load.

In this configuration shown in Fig. 4.7, only half of the noise current generated by the device under test was measured by the system. Therefore, the actual noise power was four times the measured value, and all our data were corrected by this factor. We have subtracted the thermal noise floor from our data to obtain the actual device noise. The noise of the device was measured at various bias voltages. With known total current and gain at every bias point, the excess noise factor F was then extracted as a function of the gain M as,

$$2eI_{ph0}M^2F(M) \le -171dBm/Hz \tag{4.1}$$

where I_{ph0} is the primary photocurrent at 0-bias voltage and M is the multiplication gain. Fig. 4.8 shows the measured excess noise of the CEP device and a state-of-art

Si avalanche photodetector. Limited by the noise of the instrument itself, only the results above the instrument noise floor are included in Fig 4.8. The excess noise of the state-of-the-art Si Avalanche photodiodes (APD) rises rapidly with the gain, and the measured results agree well with the McIntyre model. In contrast, the CEP device shows a significantly lower excess noise than Si APD. The excess noise factor is as low as 1.33 at a gain of 2419, which is about 30 times lower than the excess noise of conventional APD, the most sensitive semiconductor device know today.

Signal analyzer (HP 89410A) is also used to confirm the excess noise factor. The measurements were performed using the signal analyzer with a pre-amplifier (Transimpedance amplifier) system as shown in Fig. 4.9. A 1310 nm laser is used as illumination source and coupled to a tapered fiber with beam size only 2 μm, and the light is modulated by the function generator from 500 Hz to 3 kHz in the measurement. The device is electrically connected to a current transimpedance amplifier with sensitivity of 5 μA/V and reverse DC bias. The signal after the pre-amplifier is connected to the signal analyzer.

The total noise power density, N_{total}, includes the noise power contributed from dark current (I_d) and the photocurrent (I_{ph}) ,and the other noise source (N_{other}), as,

$$N_{total} = 2eI_{ph0}M_p^2F_p + 2eI_{d0}M_d^2F_d + N_{other} = 2eI_{ph}M_pF_p + 2eI_dM_dF_d + N_{other} \qquad (4.2)$$

where M_p is the multiplication gain of the photocurrent, which can be obtained from the light on measurement when the light is on at specific bias and 0-bias. The dark current noise can also be measured when the laser light is off,

$$N_{dark} = 2eI_d M_d F_d + N_{other} \tag{4.3}$$

The noise power contributed by photocurrent can be extracted,

$$N_{photo} = N_{total} - N_{dark} = 2eI_{ph} M_p F_p \tag{4.4}$$

Then the excess noise factor, F_p, can be obtained,

$$F_p = \frac{N_{total} - N_{dark}}{2eI_{ph} M_p} \tag{4.5}$$

The results of the photo noise power spectral density and the calculated excess noise factor are shown in Table 4.1. The excess noise factor is around 3.5 when the gain around 6000.

Table 4.1: Noise power spectral density at -5V and the excess noise factor.

Frequency(Hz)	Photo Noise Power Spectral Density (A^2/Hz)	Photocurrent (A)	Gain	Excess Noise Factor
5.00E+02	1.12882E-20	1.58301E-06	6280	3.55
8.00E+02	9.88506E-21	1.47736E-06	6576	3.18
1.00E+03	9.09191E-21	1.52927E-06	6067	3.06
2.00E+03	9.40465E-21	1.33194E-06	5928	3.72

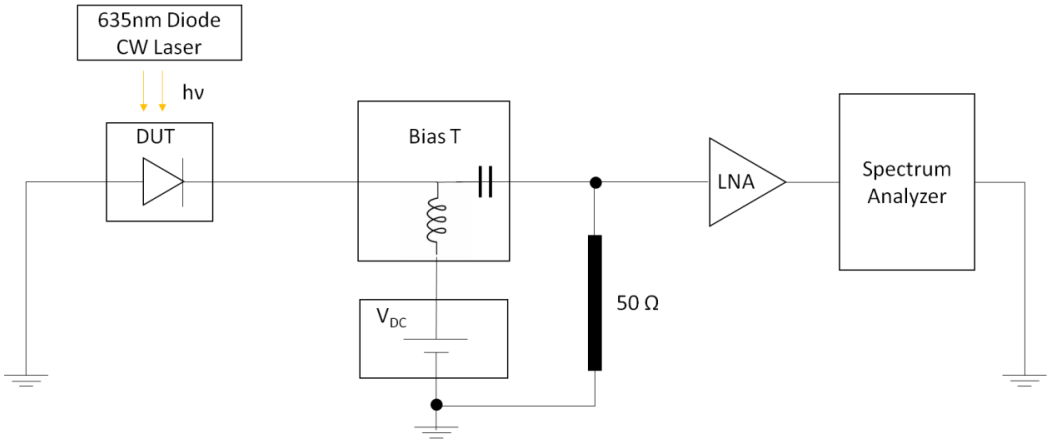

Figure 4.7: Noise measurement setup configuration with spectrum analyzer.

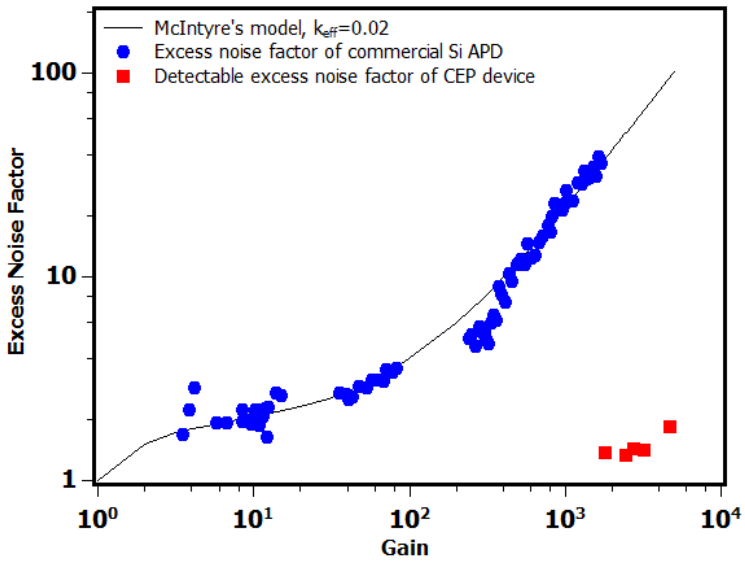

Figure 4.8: Excess noise factor. The gain dependence of excess noise factor for a state-of-the –art Si APD and the CEP device. The experimental data for the Si APD are fitted with the McIntyre model (solid curve) with K_{eff}=0.02, where K_{eff} is the ratio of hole and electron impact ionization coefficient.

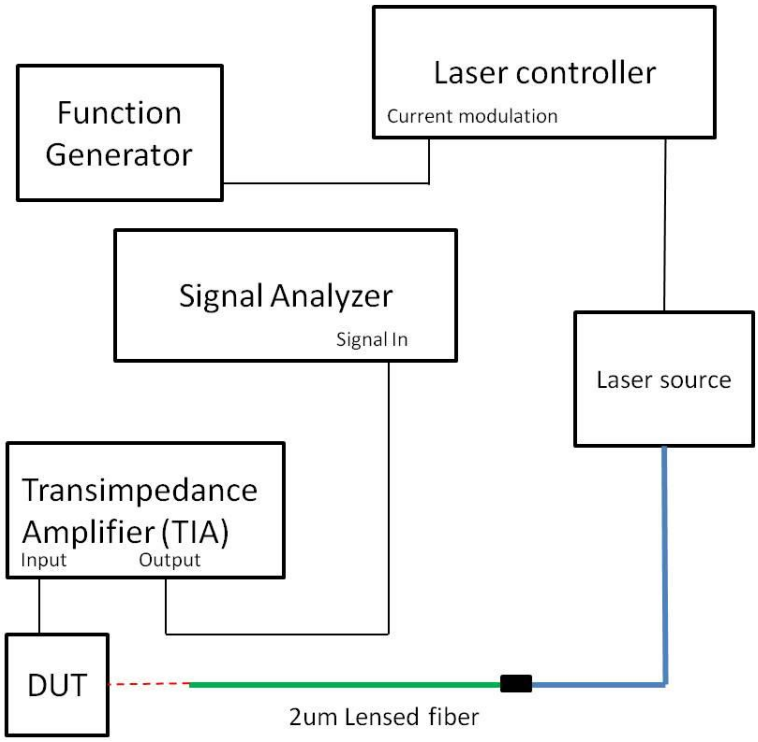

Figure 4.9: Noise measurement setup configuration with signal analyzer and fiber coupled light illumination.

4.5 Conclusion

A heavily doped and heavily compensated silicon p-n junction device that can produce the cycling excitation process to amplify signals with unprecedented efficiency and noise characteristics is demonstrated. The low bias of the device, the simple and CMOS compatible fabrication process, the favorable temperature characteristics, and the ultralow noise of the amplification process make the CEP effect a highly attractive, especially promising physical mechanism for a large family of devices beyond photodiodes which we use to prove the principle. A reasonable explanation for the CEP effect from the use of localized impurity states introduced by the compensated structure for relaxation of momentum conservation and the use of phonons to assist the amplification process is proposed. The latter is in sharp contrast with almost all known semiconductor devices where phonons lower the device performance.

Portions of this chapter have been published in Applied Physics Letter 2015 by Yu-Hsin Liu, Lujiang Yan, Alex Zhang, David Hall, Iftikhar Ahmad Niaz, Yuchun Zhou, L. J. Sham, and Yu-Hwa Lo. The dissertation author was the primary investigator and author of this paper.

Portions of this chapter have been published in the Proceedings of IEEE Photonics Conference 2015. Yu-Hsin Liu and Yu-Hwa Lo. The dissertation author was the primary investigator and author of this paper.

Chapter 5 Rate Equation Analysis for Cycling Excitation Process

5.1 Overview

Here we model the characteristics of the CEP junction by a set of rate equations, and calculate the CEP gain under steady state. The model takes into account carrier excitation from impurity states in the compensated region and the roles of phonons, including the critical phonon absorption process required for the generation of new e-h pairs and the countering process of phonon emission. The processes in Fig. 5.1 from a,b and d,e take place in sequence: (a) Primary photo generated electron excites an electron from a compensating acceptor in the n-region to the conduction band, (b) followed by a phonon absorption process to produce a hole carrier. (d) The Auger-cum-phonon created hole may similarly add an electron-hole pair from a compensating donor in the p-region. (e) The electron carrier is created by another phonon absorption. (c)(f) Phonon emission as countering process to (b,d).

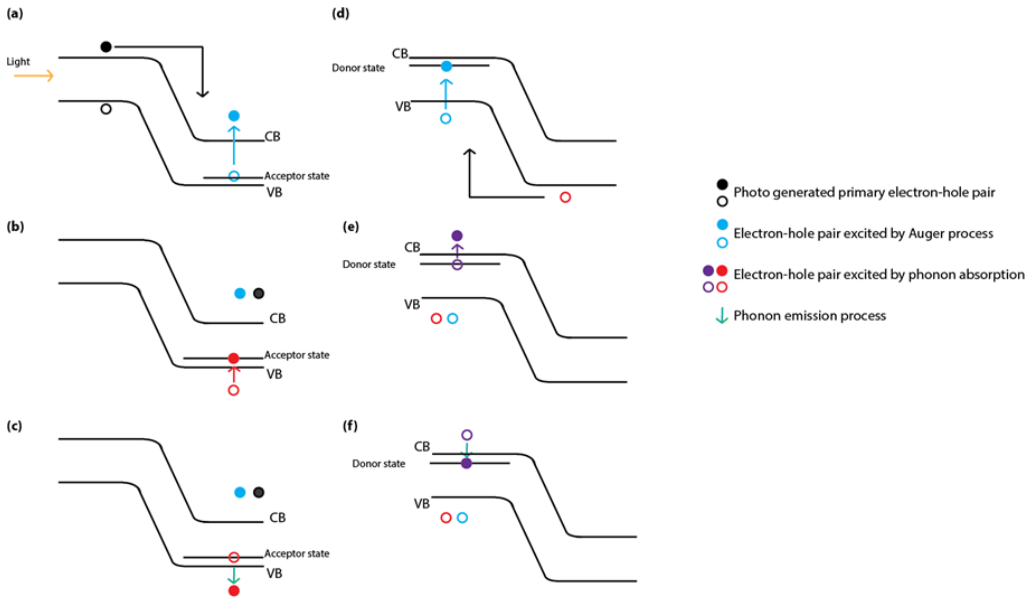

Figure 5.1: Illustration of the cycling excitation process.

5.2 Rate Equation of the Excitation Cycling Process

In the following sessions, the definitions of all constants are introduced first, and then the rate equations of carrier and dopants are discussed.

5.2.1 Definition of all Constants

p_A: Concentration (cm^{-3}) of "unoccupied" acceptors in the n-region.

n_D: Concentration (cm^{-3}) of "occupied" donors in the p-region.

p_h: Concentration (cm^{-3}) of holes in the valence band of the n-region.

n_e: Concentration (cm^{-3}) of electrons in conduction band of the p-region.

N_A: Total acceptor concentration (cm^{-3}) in the n-region.

N_D: Total donor concentration (cm^{-3}) in the p-region.

V_n: Effective volume (cm^3) in the n-region that contributes to the CEP effect.

V_p: Effective volume (cm^3) in the p-region that contributes to the CEP effect.

Ω_X: Effective volume (cm^3) of Coulomb interaction between an energetic electron and an occupied acceptor.

Ω_Y: Effective volume (cm^3) of Coulomb interaction between an energetic hole and an unoccupied donor.

τ : Single path carrier transit time (sec) across the depletion region.

τ_h: Phonon absorption time (sec) for an unoccupied acceptor in the n-region to absorb a phonon to produce a hole in the valence band.

τ_n: Phonon absorption time (sec) for an occupied donor in the p-region to absorb a phonon to produce an electron in the conduction band.

W_e : Phonon emission coefficient (cm^3/s) between electrons and the unoccupied donors in the p-region.

W_h: Phonon emission coefficient (cm^3/s) between holes and the occupied acceptors in the n-region.

5.2.2 Input Power Dependence Gain Analysis

Assume that the primary photocurrent, I_i is generated at $t = 0$ and enters the partially compensated P/N junction from the p-region. In the depletion region of junction, we can write the following rate equations for p_A, p_h n_D, and n_e as illustrated in Fig. 5.1,

$$\frac{dp_A}{dt} = \left(\frac{I_i}{qV_n} + \frac{n_e V_p}{\tau V_n}\right)(N_A - p_A)\Omega_X - \frac{p_A}{\tau_h} \qquad (5.1)$$

$$\frac{dp_h}{dt} = \frac{p_A}{\tau_h} - \frac{p_h}{\tau} - W_h(N_A - p_A)p_h \qquad (5.2)$$

$$\frac{dn_D}{dt} = \frac{p_h V_n}{\tau V_p}(N_D - n_D)\Omega_Y - \frac{n_D}{\tau_e} \qquad (5.3)$$

$$\frac{dn_e}{dt} = \frac{n_D}{\tau_e} - \frac{n_e}{\tau} - W_e(N_D - n_D)n_e \qquad (5.4)$$

We can then find the steady-state solution for p_A, n_D, p_h, n_e from equations (1) to (4). Without any input signal (i.e. $I_i = 0$), we have the trivial solution of $p_A = n_D = p_h = n_e = 0$. However, when the input current is present, the solution is rather complicated. Without losing any key features or generality of the CEP mechanism, for a simpler model, we assume all material parameters for electrons and holes are the same and symmetric as:

$N_A = N_D = N;\quad W_h = W_e = W;\quad \tau_e = \tau_h = T;\quad \Omega_X = \Omega_Y = \Omega;\quad V_n = V_p = V.$

Hence, at steady state, we have the simplified rate equations, if input current is from p-side only,

$$\left(\frac{I_i}{qV} + \frac{n_e}{\tau}\right)(N - p_A)\Omega - \frac{p_A}{T} = 0 \qquad (5.5)$$

$$\frac{p_A}{T} - \frac{p_h}{\tau} - W(N - p_A)p_h = 0 \qquad (5.6)$$

$$\frac{p_h}{\tau}(N - n_D)\Omega - \frac{n_D}{T} = 0 \qquad (5.7)$$

$$\frac{n_D}{T} - \frac{n_e}{\tau} - W(N - n_D)n_e = 0 \qquad (5.8)$$

The current across the junction and Gain are defined as,

$$\frac{I_o}{qV} = \frac{I_i}{qV} + \frac{n_e}{\tau} + \frac{p_h}{\tau} \quad \Leftrightarrow \quad I_o = I_i + qV\left(\frac{n_e}{\tau} + \frac{p_h}{\tau}\right) \tag{5.9}$$

$$Large\ signal\ Gain:\ \ G = \frac{I_0}{I_i} = 1 + \frac{qV}{I_i}\left(\frac{n_e}{\tau} + \frac{p_h}{\tau}\right) \tag{5.10}$$

$$Differential\ \ Gain:\ \ g = \frac{dI_0}{dI_i} = 1 + qV\frac{d}{dI_i}\left(\frac{n_e}{\tau} + \frac{p_h}{\tau}\right) \tag{5.11}$$

$Define\ that\ x = \frac{n_e}{\tau}\ and\ y = \frac{p_h}{\tau}\ then\ we\ have,$

$$Large\ signal\ Gain:\ \ G = 1 + \frac{qV}{I_i}(x + y) \tag{5.12}$$

$$Differential\ \ Gain:\ \ g = \frac{dI_0}{dI_i} = 1 + qV\frac{d}{dI_i}(x + y) \tag{5.13}$$

Therefore, equations (5) to (8) become,

$$\left(\frac{I_i}{qV} + x\right)(N - p_A)\Omega = \frac{p_A}{T} \tag{5.14}$$

$$\frac{p_A}{T} - y - W(N - p_A)\tau y = 0 \tag{5.15}$$

$$y(N - n_D)\Omega = \frac{n_D}{T} \tag{5.16}$$

$$\frac{n_D}{T} - x - W(N - n_D)\tau x = 0 \tag{5.17}$$

From (15) and (17), we can find,

$$p_A = \frac{(1+WN\tau)Ty}{1+WT\tau y} \tag{5.18}$$

$$n_D = \frac{(1+WN\tau)Tx}{1+WT\tau x} \tag{5.19}$$

Substitute (18) and (19) into (14) and (16).

$$Assume\ constants:\ \ A = \frac{1+WN\tau}{N\Omega};\ \ B = \frac{T}{N};\ \ C = \frac{I_i}{qV}$$

Solve (18) (19) for *x* and *y*,

$$x = \frac{1-A-BC}{2B} + \sqrt{\left(\frac{A+BC-1}{2B}\right)^2 + \frac{C}{(A+1)B}} \tag{5.20}$$

$$y = \frac{1-A}{2B} + \sqrt{\left(\frac{A-1}{2B}\right)^2 + \frac{AC}{B(1+A+BC)}} \tag{5.21}$$

From (12), we can find the large signal gain as,

$$G = 1 + \frac{qV}{I_i}(x+y) = 1 + \frac{x+y}{C}$$

$$G = \frac{1}{2} + \frac{1-A}{BC} + \sqrt{\left(\frac{A+BC-1}{2BC}\right)^2 + \frac{1}{(A+1)BC}} + \sqrt{\left(\frac{A-1}{2BC}\right)^2 + \frac{A}{BC(1+A+BC)}} \tag{5.22}$$

From (13), we can get the differential gain,

$$g = \frac{dI_0}{dI_i} = 1 + qV\frac{d}{dI_i}(x+y) = G + BC \cdot \frac{dG}{d(BC)}$$

Further define $z = BC$, we can write the gain in terms of z,

$$G(z) = \frac{1}{2} + \frac{1-A}{z} + \sqrt{\frac{1}{4} + \frac{A^2+1}{2A+2}\cdot\frac{1}{z} + \left(\frac{A-1}{2}\right)^2\frac{1}{z^2}} + \sqrt{\left(\frac{A-1}{2}\right)^2\frac{1}{z^2} + \frac{A}{1+A+z}\cdot\frac{1}{z}} \tag{5.23}$$

$$g(z) = G + z \cdot \frac{dG}{dz} \tag{5.24}$$

To get a more concise expression of the CEP gain, we will examine the input current injection level to get an estimate of z and then simplify G based on the z value range.

$$I_s = \frac{qNV}{T}\ as\ a\ reference\ current.\quad Then,\qquad z = BC = \frac{T}{qNV}\cdot I_i = \frac{I_i}{I_s}$$

From the dimension of our CEP device, the volume of one side of the depletion region is,

$$V \sim 35\mu m \times 55\mu m \times 10nm = 35 \times 10^{-4} \times 55 \times 10^{-4} \times 10 \times 10^{-7}$$
$$= 1.925 \times 10^{-11}\ (cm^3)$$

We estimate $T \approx 25(ps)$ for effective phonon absorption time[35]. Therefore the reference current can be calculated as,

$$I_s = \frac{qNV}{T} = \frac{1.602 \times 10^{-19} \times 2 \times 10^{19} \times 1.925 \times 10^{-11}}{25 \times 10^{-12}} = 2.5\ (Amps)$$

This reference current value is huge compare to the current injection level in our measurements, which is on the order of nano-ampere. Therefore, all the measurements were assumed to be done under low current injection condition.

$i.e.\ I_i \ll I_s \Rightarrow\ \ z = \frac{I_i}{I_s} \ll 1$

Re-arrange equation (23) also considering $z \ll 1$

$$G(z) = \frac{1}{2} + \frac{1-A}{z} + \left|\frac{A-1}{2} \cdot \frac{1}{z}\right| \left\{\sqrt{1 + \frac{A^2+1}{2A+2} \cdot \left(\frac{2}{A-1}\right)^2 \cdot z + \frac{1}{4} \cdot \left(\frac{2}{A-1}\right)^2 \cdot z^2} + \right.$$

$$1+2A-12\cdot A1+A+z\cdot z \qquad (5.25)$$

$$Define, \qquad f(z) = \sqrt{1 + \frac{2(A^2+1)}{(A+1)(A-1)^2} \cdot z + \frac{1}{(A-1)^2} \cdot z^2}$$

$$Define, \qquad h\,(z) = \sqrt{1 + \left(\frac{2}{A-1}\right)^2 \cdot \frac{A}{1+A+z} \cdot z}$$

$$G(z) = \frac{1}{2} + \frac{1-A}{z} + \left|\frac{A-1}{2} \cdot \frac{1}{z}\right| \cdot [f(z) + h(z)] \qquad (5.26)$$

Apply Taylor series expansion on $f(z)$

$f(z) = \sum_{n=0}^{\infty} \frac{f^{(n)}(0)}{n!} z^n = f(0) + \frac{f^{(1)}(0)}{1!} \cdot z + \frac{f^{(2)}(0)}{2!} \cdot z^2 + \cdots$

The coefficients are calculated as,

$f(0) = 1$

$$f^{(1)}(0) = \frac{A^2+1}{(A+1)(A-1)^2}$$

$$f^{(2)}(0) = \frac{-4A^2}{(A+1)^2(A-1)^4}$$

Under the low input current injection condition, i.e. $z \ll 1$, we keep up to the second order terms,

$$f(z) \cong f(0) + \frac{f^{(1)}(0)}{1!} \cdot z + \frac{f^{(2)}(0)}{2!} \cdot z^2 = 1 + \frac{A^2+1}{(A+1)(A-1)^2} \cdot z - \frac{2A^2}{(A+1)^2(A-1)^4} \cdot$$

$z^2 \qquad (5.27)$

Similarly, the coefficients of Taylor expansion of $h(z)$ is calculated as,

$$h(0) = 1$$

$$h^{(1)}(0) = \frac{2A}{(A+1)(A-1)^2}$$

$$h^{(2)}(0) = -\frac{4A^2 + 4A(A-1)^2}{(A+1)^2(A-1)^4}$$

$$h(z) \cong h(0) + \frac{h^{(1)}(0)}{1!} \cdot z + \frac{h^{(2)}(0)}{2!} \cdot z^2 = 1 + \frac{2A}{(A+1)(A-1)^2} \cdot z - \frac{2A^2+2A(A-1)^2}{(A+1)^2(A-1)^4} \cdot z^2 \quad (5.28)$$

Therefore,

$$f(z) + h(z) = 2 + \frac{A+1}{(A-1)^2} \cdot z - \frac{4A^2+2A(A-1)^2}{(A+1)^2(A-1)^4} \cdot z^2 \quad (5.29)$$

Based on the simple symmetric model we used, term A must be larger than 1. Which means the value of Ω cannot exceed $(1/N + W\tau)$. Physically, it demands that the effective Coulomb interactive volume cannot be greater than the space between the compensating dopant atoms plus the effective volume which compensates for the loss of carriers by phonon emission. Otherwise the probability of an injected carrier to excite another carrier from the compensating dopant will be larger than 1, and gain will explode which is not observed. As $A > 1$, from (23) and (24),

$$G(z) = \frac{1}{2} + \frac{1-A}{z} + \left|\frac{A-1}{2} \cdot \frac{1}{z}\right| \cdot [f(z) + h(z)]$$

$$= \frac{1}{2} + \frac{1-A}{z} + \frac{A-1}{2z} \cdot \left[2 + \frac{A+1}{(A-1)^2} \cdot z - \frac{4A^2 + 2A(A-1)^2}{(A+1)^2(A-1)^4} \cdot z^2\right]$$

$$= \frac{A}{A-1} - \frac{A(A^2+1)}{(A+1)^2(A-1)^3} \cdot z$$

Re-write the expression, we have,

$$Large\ signal\ gain: G(z) = 1 + \frac{1}{A-1} - \frac{A(A^2+1)}{(A+1)^2(A-1)^3} \cdot z \quad (5.30)$$

$$g(z) = G + z \cdot \frac{dG}{dz} = \frac{A}{A-1} - \frac{A(A^2+1)}{(A+1)^2(A-1)^3} \cdot z + z \cdot \left[-\frac{A(A^2+1)}{(A+1)^2(A-1)^3}\right]$$

Simplify the expression, we have,

$$Differential\ gain: g(z) = 1 + \frac{1}{A-1} - \frac{2A(A^2+1)}{(A+1)^2(A-1)^3} \cdot z \tag{5.31}$$

The differential gain of a CEP junction can be written, from (34), as

$$g_{CEP} = 1 + \frac{1}{A-1} - \frac{2A(A^2+1)}{(A+1)^2(A-1)^3} \cdot \frac{I_i}{I_s} \tag{5.32}$$

$$where\ A = \frac{1 + WN\tau}{N\Omega} \quad and \quad I_s = \frac{qNV}{T} \approx 2.5(A)$$

The gain increases with the decreasing primary photocurrent as seen in Eq. (5.32), which is also measured and shown in Fig. 4.5 and Fig. 4.6. With higher temperature, the effective phonon absorption time is reduced. As Eq. (5.32), as T decreases, the reference current I_s increase, therefore the gain will increase. This is also measured and shown in Fig. 4.7.

The model also shows high gain is reached when voltage dependent them "A" is very closed to 1[36]. This yields the defined effective CEP volume "Ω" to approach the maximum value of $\frac{1}{N} + W\tau$, which means the effective CEP volume quickly saturate at -3V and every hot electron can see the whole cross-section of the compensating dopant, $\frac{1}{N}$, for coulomb interaction to produce new carriers.

5.2.3 Frequency Response

In this part of the model, we analyze the characteristics of the CEP junction by the same set of rate equations, but under time-varying input signal (modulated incident light intensity). The primary input current is a small time varying part plus a DC bias. They are denoted as below,

$$I_i = I_{i0} + \Delta I_i \cdot e^{j\omega t} \tag{5.33}$$

Thus some non-constant carrier concentrations, as a result, can be expressed as,

$$n_e = n_{e0} + \Delta n_e \cdot e^{j\omega t} \tag{5.34}$$

$$p_h = p_{h0} + \Delta p_h \cdot e^{j\omega t} \tag{5.35}$$

$$n_D = n_{D0} + \Delta n_D \cdot e^{j\omega t} \tag{5.36}$$

$$p_A = p_{A0} + \Delta p_A \cdot e^{j\omega t} \tag{5.37}$$

Define the output current of the CEP junction as,

$$I_{out} = I_{out0} + \Delta I_{out} \cdot e^{j\omega t} \tag{5.38}$$

From the output current defined in equation (9), we also know,

$$\begin{aligned} I_{out} &= I_i + qV\left(\frac{n_e}{\tau} + \frac{p_h}{\tau}\right) \\ &= \left(I_{i0} + \Delta I_i \cdot e^{j\omega t}\right) + \frac{qV}{\tau}\left[\left(n_{e0} + \Delta n_e \cdot e^{j\omega t}\right) + \left(p_{h0} + \Delta p_h \cdot e^{j\omega t}\right)\right] \\ &= \left[I_{i0} + \frac{qV}{\tau}(n_{e0} + p_{h0})\right] + e^{j\omega t} \cdot \left[\Delta I_i + \frac{qV}{\tau}(\Delta n_e + \Delta p_h)\right] \end{aligned}$$

And by comparing the time dependent and independent coefficients,

$$\mathrm{I_{out0}} = \mathrm{I_{i0}} + \frac{\mathrm{qV}}{\tau}(\mathrm{n_{e0}} + \mathrm{p_{h0}}) \tag{5.39}$$

$$\Delta\mathrm{I_{out}} = \Delta\mathrm{I_i} + \frac{\mathrm{qV}}{\tau}(\Delta\mathrm{n_e} + \Delta\mathrm{p_h}) \tag{5.40}$$

And then the gain can be defined as,

$$\text{DC Gain:}\quad \mathrm{G} = \frac{\mathrm{I_{out0}}}{\mathrm{I_{i0}}} = 1 + \frac{\mathrm{qV}}{\mathrm{I_{i0}}}\left(\frac{\mathrm{n_{e0}}}{\tau} + \frac{\mathrm{p_{h0}}}{\tau}\right) \tag{5.41}$$

$$\text{Small Signal Gain:}\quad \mathrm{g} = \frac{\Delta\mathrm{I_{out}}}{\Delta\mathrm{I_i}} = 1 + \frac{\mathrm{qV}}{\Delta\mathrm{I_i}}\left(\frac{\Delta\mathrm{n_e}}{\tau} + \frac{\Delta\mathrm{p_h}}{\tau}\right) \tag{5.42}$$

The DC gain is what was found in equation (5.32) of 5.2.2, which is independent of time. In fact all the time-independent parameters are determined in

5.2.2, It is the frequency (time) dependent small signal gain, $g(\omega)$, that we are going to determine.

Denote the intermediate constants and parameters as,

$$x = \frac{n_e}{\tau} = x_0 + \Delta x \cdot e^{j\omega t} = \frac{n_{e0}}{\tau} + \frac{\Delta n_e}{\tau} \cdot e^{j\omega t} \tag{5.43}$$

$$y = \frac{p_h}{\tau} = y_0 + \Delta y \cdot e^{j\omega t} = \frac{p_{h0}}{\tau} + \frac{\Delta p_h}{\tau} \cdot e^{j\omega t} \tag{5.44}$$

$$C = \frac{I_i}{qV} = C_0 + \Delta C \cdot e^{j\omega t} = \frac{I_{i0}}{qV} + \frac{\Delta I_i}{qV} \cdot e^{j\omega t} \tag{5.45}$$

Where

$$\begin{cases} x_0 = \dfrac{n_{e0}}{\tau} \\ \Delta x = \dfrac{\Delta n_e}{\tau} \end{cases}; \quad \begin{cases} y_0 = \dfrac{p_{h0}}{\tau} \\ \Delta y = \dfrac{\Delta p_h}{\tau} \end{cases}; \quad \begin{cases} C_0 = \dfrac{I_{i0}}{qV} \\ \Delta C = \dfrac{\Delta I_i}{qV} \end{cases}$$

$$Small\ Signal\ Gain:\ \ g = \frac{\Delta I_{out}}{\Delta I_i} = 1 + \frac{qV}{\Delta I_i}\left(\frac{\Delta n_e}{\tau} + \frac{\Delta p_h}{\tau}\right) = 1 + \frac{\Delta x + \Delta y}{\Delta C} \tag{5.46}$$

Substitute Eq. (5.34) to (5.37) into Eq. (5.1) to (5.4), apply similar analysis following the steps of 1) Substitute all small signal expression into the equation; 2) Expand the equation and re-arrange with the power of $e^{j\omega t}$; 3) Simplify the equation by subtracting the DC model equation and by taking small signal amplitude square to be negligible; 4) Eliminate the phasor term. After the algebra, we have,

$$j\omega \cdot \Delta p_A = \left(\frac{\Delta I_i}{qV} + \frac{\Delta n_e}{\tau}\right)(N - p_{A0})\Omega_X - \left(\frac{I_{i0}}{qV} + \frac{n_{e0}}{\tau}\right)\Delta p_A \Omega_X - \frac{\Delta p_A}{T} \tag{5.47}$$

$$j\omega \cdot \Delta p_h = \frac{\Delta p_A}{T} - \frac{\Delta p_h}{\tau} - W[(N - p_{A0})\Delta p_h - \Delta p_A p_{h0}] \tag{5.48}$$

$$j\omega \cdot \Delta n_D = \frac{\Delta p_h}{\tau}(N - n_{D0})\Omega_Y - \frac{p_{h0}}{\tau}\Delta n_D \Omega_Y - \frac{\Delta n_D}{T} \tag{5.49}$$

$$j\omega \cdot \Delta n_e = \frac{\Delta n_D}{T} - \frac{\Delta n_e}{\tau} - W[(N - n_{D0})\Delta n_e - \Delta n_D n_{e0}] \tag{5.50}$$

Assume that $WN\tau \approx 0.05 \ll 1$. Then it follows,

$$WN\tau \ll 1 \quad \Rightarrow \quad WN \ll \frac{1}{\tau} \quad \Rightarrow \quad \frac{\Delta p_h}{\tau} \gg \Delta p_h WN > \Delta p_h W(N - p_{A0})$$

$$\frac{\Delta p_h}{\tau} \gg W[(N - p_{A0})\Delta p_h - \Delta p_A p_{h0}]$$

Therefore, the term $W[(N - p_{A0})\Delta p_h - \Delta p_A p_{h0}]$ can actually be neglected from equation (5.48). For simplicity and a more concise model of $g(\omega)$, the effect of phonon emission is ignored here by taking the assumption that $W \to 0$. Then we can re-write the equation (5.47) to (5.50) as,

$$j\omega \cdot \Delta p_A = \left(\frac{\Delta I_i}{qV} + \frac{\Delta n_e}{\tau}\right)(N - p_{A0})\Omega_X - \left(\frac{I_{i0}}{qV} + \frac{n_{e0}}{\tau}\right)\Delta p_A \Omega_X - \frac{\Delta p_A}{T} \tag{5.51}$$

$$j\omega \cdot \Delta p_h = \frac{\Delta p_A}{T} - \frac{\Delta p_h}{\tau} \tag{5.52}$$

$$j\omega \cdot \Delta n_D = \frac{\Delta p_h}{\tau}(N - n_{D0})\Omega_Y - \frac{p_{h0}}{\tau}\Delta n_D \Omega_Y - \frac{\Delta n_D}{T} \tag{5.53}$$

$$j\omega \cdot \Delta n_e = \frac{\Delta n_D}{T} - \frac{\Delta n_e}{\tau} \tag{5.54}$$

Using the denotations for x,y, and C defined previously, Eq (5.51) to (5.54) can be rewritten as,

$$\left[j\omega + (C_0 + x_0)\Omega_X + \frac{1}{T}\right] \cdot \Delta p_A = (\Delta C + \Delta x)(N - p_{A0})\Omega_X \tag{5.55}$$

$$j\omega\tau \cdot \Delta y = \frac{\Delta p_A}{T} - \Delta y \tag{5.56}$$

$$\left[j\omega + y_0\Omega_Y + \frac{1}{T}\right] \cdot \Delta n_D = \Delta y(N - n_{D0})\Omega_Y \tag{5.57}$$

$$j\omega\tau \cdot \Delta x = \frac{\Delta n_D}{T} - \Delta x \tag{5.58}$$

Solve Eq. (5.55) to (5.58), and the small signal gain in (5.46) can be obtained,

$$g = \frac{\Delta I_{out}}{\Delta I_i} = 1 + \frac{qV}{\Delta I_i}\left(\frac{\Delta n_e}{\tau} + \frac{\Delta p_h}{\tau}\right) = 1 + \frac{\Delta x}{\Delta C} + \frac{\Delta y}{\Delta C} \tag{5.46}$$

$$g(\omega) = 1 + \frac{\alpha_1\beta_0\beta_2 + \alpha_1\alpha_2}{\beta_0^2\beta_1\beta_2 - \alpha_1\alpha_2} = \frac{\alpha_1\beta_0\beta_2 + \beta_0^2\beta_1\beta_2}{\beta_0^2\beta_1\beta_2 - \alpha_1\alpha_2} \tag{5.59}$$

$$\text{Where } \begin{cases} \alpha_1 = (N - y_0 T)\cdot \Omega_X \\ \alpha_2 = (N - x_0 T)\cdot \Omega_Y \end{cases}; \quad \begin{cases} \beta_0 = 1 + j\omega\tau \\ \beta_1 = 1 + j\omega T + (C_0 + x_0)\Omega_X T \\ \beta_2 = 1 + j\omega T + y_0 \Omega_Y T \end{cases}$$

The x_0 and y_0 values are calculated in equation (5.20) and (5.21) in 5.2.2. The frequency dependent gain is shown in the Fig. 5.2 (Courtesy of Lujiang Yan). The gain can reach to 10^7 and above if the input current decreases to 1pA. The trend between the gain and the input current also agrees with the observation from experimental results in 4.3.2. The frequency dependence also illustrates the bandwidth around 10 MHz of the CEP devices.

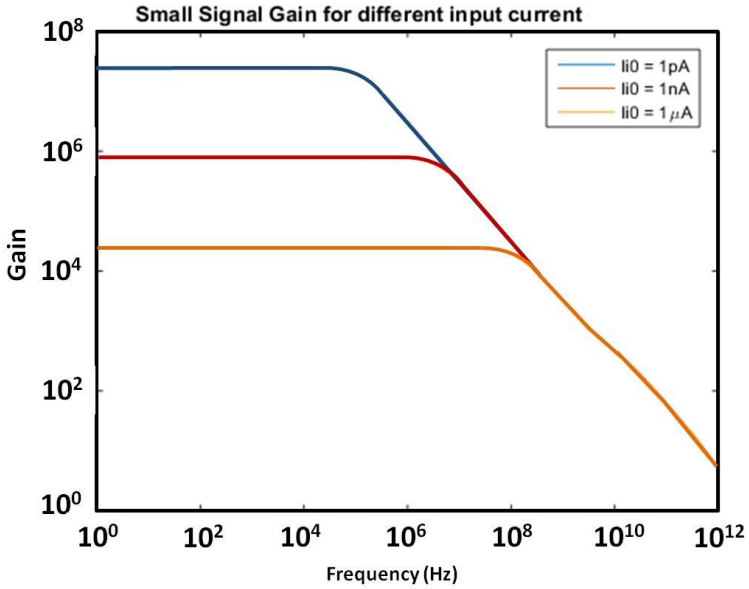

Figure 5.2: Small signal gain for different input current.

5.3 Conclusion

The rate equation model on the CEP p-n junction predicts the gain decreases with increasing input power, temperature dependence, also the gain saturation with increasing voltage. The small signal analysis also illustrates the input current dependence, which agrees with the experimental results in Chapter 4.

Portions of this chapter have been published in Applied Physics Letter 2015 by Yu-Hsin Liu, Lujiang Yan, Alex Zhang, David Hall, Iftikhar Ahmad Niaz, Yuchun Zhou, L. J. Sham, and Yu-Hwa Lo. The dissertation author was the primary investigator and author of this paper.

The author thanks Lujiang Yan for use of Fig. 5.2.

Chapter 6 Conclusion

Heavily doped p-n junction devices have been studied for enhancing the sub-bandgap absorption coefficient and the signal amplification of pure silicon. Highly doped impurity bands help to relax the k-selection rule for indirect bandgap materials. The electron transitions between the impurity band and the conduction/valence band are much efficient than band-to-band transitions.

The waveguide-coupled epitaxial p-n photodetector device was demonstrated for 1310 nm wavelength detection. Incorporated with the Franz-Keldysh effect and the quasi-confined epitaxial layer design, an absorption coefficient of around 10/cm has been measured for our device.

To solve the issues of large excess noise and high operation bias for avalanche photodiodes based on impact ionization, I presented a detector using the Cycling Excitation Process (CEP) for signal amplification. This can be realized in a heavily doped and highly compensated Si p-n junction, showing ultra high gain at very low bias (<4 V), and possessing an intrinsic, phonon-mediated regulation process to keep the device stable without any quenching device required in today's Geiger-mode avalanche detectors.

6.1Outlook

The higher dark current, due to the multiplication process, has been observed in my CEP devices. Based on simulations of the intrinsic spacer layers in between

the p-n junction in compensated layers, the dark current can be suppressed. The passivation layer is also important to avoid surface/interface defects or inversion surface junctions. The qualities of the passivation layers can be analyzed from CV measurements.

The uniformity of gain is important for array applications such as imaging. A 2-D mapping of an array of devices can be performed. A tapered fiber with 2 μm diameter beam size can be used for light illumination inside each device. The gain uniformity in the device and between each device can be analyzed by moving the fiber tip.

Other than the above characterizations for the current CEP devices, the mechanism can also be applied in the following fields.

6.1.1 Other Semiconductor Materials

CEP can be applied to other semiconductor materials for different applications. We have collaborated with others on GaAs photodetectors and characterize the external quantum efficiency (EQE) also the dark current properties

The CEP junction in Si incorporated with Ge epitaxial layers also has been designed for IR detection applications. The light absorption region in this case is separated from the multiplication region. 50 um-disk devices have been fabricated and preliminary results show that the photocurrent gain increases with reverse bias and decreases with increasing input laser power.

6.1.2 Imaging System Application

The photodetector at the heart of most CMOS image sensors is a photodiode. The imaging performance depends on the application. For example, biological fluorescence imaging requires the dark current to be minimized. Besides, increasing incident light intensity is not advisable since it causes rapid photobleaching. Thus, a photodiode with high sensitivity is favorable. CEP photodiodes with intrinsic gain characteristics and low operation bias could be a new option to replace the conventional photodiodes in a pixel, and even substitute the amplifying functions of transimpedance amplifiers[37-41].

6.1.3 Single Photon Detection

Single photon detectors traditionally use impact ionization as an internal gain mechanism. There are several constraints that limit the performance of these devices, such as device lifetime and reliability due to the high operating bias. With CEP, the device can be operated at lower reverse bias and the intrinsic gain controlled by phonon dynamics acts as a quenching mechanism.

Detection efficiency is an important figure of merit for a photodetector with sensitivity approaching single photon. The detection efficiency (DE) is the probability of a detection event, where a detection event is defined as an output signal amplitude from the device that is greater than a predetermined threshold value. For a packet of multiple photons, the detection efficiency is the probability of at least one of these input photons triggering a detection event. In the limit of a single input

photon, the detection efficiency becomes the single photon detection efficiency (SPDE) and is defined as the probability of a single incident photon triggering a detection event.

Because a true single photon source is often not available, a pulsed laser with attenuation is used. The attenuation reduces the average power to correspond to an output of less than one photon per pulse on average. Because the number of photons contained in the laser beam follows a Poisson distribution, it is possible that a pulse can produce a single photon even if the pulse contains less than one photon per pulse on average.

. The probability of obtaining k photons in a pulse when the average number of photons per pulse is n is:

$$P(k,n) = \frac{n^k e^{-n}}{k!} \tag{6.1}$$

When n is sufficiently less than 1, there will be a non-negligible probability of obtaining a single photon, but a negligible probability of obtaining two or more photons. Based on the above definition of detection efficiency, we can compute the DE:

$$DE = \sum_{k=0}^{\infty} P(k,n)\,[1-(1-SPDE)^k] \tag{6.2}$$

$$DE = \sum_{k=0}^{\infty} \frac{n^k e^{-n}}{k!}\,[1-(1-SPDE)^k] \tag{6.3}$$

Since the sum over the Poisson distribution for all k is 1, we have

$$DE = 1 - \sum_{k=0}^{\infty} \frac{[n(1-SPDE)]^k e^{-[n(1-SPDE)]}}{k!}\, e^{-n\cdot SPDE} \tag{6.4}$$

Let $n' = n(1 - SPDE)$, and we have another Poisson distribution, which yields 1 when summed over all k. Then, we can expand the remaining exponential in a power series and keep the first order terms provided n<<1.

$$DE = 1 - e^{-n \cdot SPDE} \cong 1 - (1 - n \cdot SPDE) = n \cdot SPDE \quad (6.5)$$

The single photon detection efficiency (SPDE) and dark count rate (DCR) of the device is measured using time correlated single photon counting. An external pulse generator triggers a high speed counter and a pulsed pico-second laser simultaneously[42-45], while the counter records the delay between the laser trigger and the device's pulse signal. Any counts that are not correlated with the laser pulses are considered as dark counts or after-pulses. The SPDE is obtained from the ratio of the correlated pulse counts and the number of laser pulses, after taking into account the Poisson characteristics of the laser pulses.

References

1. Chuang, S. Lien, *Physics of Optoelectronic Devices*. N.Y.: John Wiley & Sons, Inc., 1995

2. Sze, S.M, *Semiconductor Devices Physics and Technology*. N.Y.: John Wiley & Sons, Inc., 2001

3. Pallab, B., *Semiconductor Optoelectronic Devices*. N. J.: Prentice Hall International, Inc., 1996

4. Didomenico, M. and Svelto, O., "Solid-State Photodetection: A Comparison between Photoconductors and Photodiodes," *Proceedings of the IEEE*, pp. 136-144, February 1964.

5. Döhler, G. H., "The physics and applications of n-i-p-i doping superlattices," *Critical Reviews in Solid State and Materials Sciences*, Vol. 13:2, pp. 97-141, 1986.

6. Street, R. A., Döhler, G. H., Miller, J. N., and Ruden, P. P., "Luminescence of n-i-p-I heterostructures," *Phys. Rev. B* 33, pp. 7043-7046, 1986.

7. Yotter, R.A., and Wilson, D.M., "A Review of Photodetectors for Sensing Light-Emitting Reporters in Biological Systems," *IEEE SENSORS JOURNAL, 3*, pp. 288-303, 2003.

8. Mclntyre, R. J., "Multiplication noise in uniform avalanche diodes," IEEE Trans. Electron Devices ED-13, pp. 164-168, 1966.

9. Assefa, F., and Vlasov, Y. A., "Reinventing germanium avalanche photodetector for nanophotonic on-chip optical interconnects," *Nature* 464, 80, 2010.

10. Wegrzecka, I., Wegrzecki, M., Grynglas, M., Bar, J., Uszynski, A., Grodecki, R., Grabiec, P., Krzeminski, S., and Budzynski, T., "Design and Properties of Silicon Avalanche Photodiodes," *OPTO-ELECTRONICS REVIEW* 12, 95–104, 2004.

11. Michel, J., Liu, J., and Kimerling, L. C., "High-performance Ge-on-Si photodetectors," *Nature Photon*. 4, 527, 2010.

12. Zhao, K., Zhang, A., Kang, Y.M., Lo, Y.H, "InGaAs/InP MOS single photon detector," Conference Proceedings - Lasers and Electro-Optics Society Annual Meeting-LEOS, 2006.

13. Casalino, M., Coppola, G., Iodice, M., Rendina, I., and Sirleto, L., "Near-Infrared Sub-Bandgap All-Silicon Photodetectors: State of the Art and Perspectives," Sensors, 10, pp. 10571-10600, 2010.

14. Fan, H. Y., and Ramdas, A. K., "Infrared Absorption and Photoconductivity in Irradiated Silicon," *Journal of Applied Physics* 30, 1127, 1959.

15. Libertino, S., Benton, J., and Coffa, S., "Formation, evolution, and annihilation of interstitial clusters in ion-implanted Si," *Phys. Rev. B* 63, 195206, 2001.

16. Geis, M.W., Spector, S.J., Grein, M.E., Schulein, R.T., Yoon, J.U., Lennon, D.M., Denault, S., Gan, F., Kaertner, F.X., and Lyszczarz, T.M., "CMOS-compatible all-Si high-speed waveguide photodiodes with high responsivity in near-infrared communication band," *IEEE Photon. Technol. Lett. 19*, pp. 152-154, 2007.

17. Zhang, A., You, S., Soci, C., Liu, Y., Wang, D., and Lo, Y. H., "Silicon nanowire detectors showing phototransistive gain," *Appl. Phys. Lett*. **93**, 121110, 2008.

18. Zhang, A., Kim, H., Cheng, J., and Lo, Y.H., "Ultrahigh responsivity visible and infrared detection using silicon nanowire phototransistors," *Nano Lett*. **10**, 2117 (2010)

19. Soci, C., Zhang, A., Bao, X. Y., Kim, H., Lo, Y.H., and Wang, D., "Nanowire photodetectors,"*J. Nanosci. Nanotech.* **10**, 1 (2010)

20. Doylend, J. K., Jessop, P. E., and Knights, A. P., "Silicon photonic resonator-enhanced defect-mediated photodiode for sub-bandgap detection," *Opt. Express* 18, pp. 14671-14678, 2010.

21. Geis, M. W., Spector, S. J., Grein, M. E., Yoon, J. U., Lennon, D. M., and Lyszczarz, T. M., "Silicon waveguide infrared photodiodes with >35 GHz bandwidth and phototransistors with 50 AW-1 response," Opt. Express. **17**, pp.5193-5204, 2009.

22. Baehr-Jones, T., Hochberg, M., and Scherer, A., "Photodetection in silicon beyond the band edge with surface states," Optics Express. **16**, pp. 1659-1668, 2008.

23. Logan, D. F., Velha, P., Sorel, M., De La Rue, R. M., Knights, A. P., and Jessop, P. E., "Defect-Enhanced Silicon-on-Insulator Waveguide Resonant Photodetector With High Sensitivity at 1.55 m," IEEE Photonics Technology Lett. **22**, pp. 1530-1532, 2010.

24. Shafiiha, R., Zheng, D., Liao, S., Dong, P., Liang, H., Feng, N., Luff, B. J., Feng, D., Li, G., Cunningham, J., Raj, K., Krishnamoorthy, A. V., and Asghari, M., "Silicon waveguide coupled resonator infrared detector," Proc. of Optical Fiber Communication Conference, San Diego, USA, 2010.

25. J. Ackert, M. Fiorentino, D. F. Logan, R. G. Beausoleil, P. E. Jessop, and A. P. Knights, "Silicon-on-insulator microring resonator defect-based photodetector with 3.5-GHz bandwidth ," *Journal of Nanophotonics*. **5**, 059507, 2011.

26. Chen, H., Luo, X., Poon, A. W., "Cavity-enhanced photocurrent generation by 1.55 μm wavelengths linear absorption in a p-i-n diode embedded silicon microring resonator," *Appl. Phys. Lett.*, 95, 171111, 2009.

27. Casalino, M., Gioffrè, M., Coppola, G., Iodice, M., Moretti, L., Rendina, I., Sirleto, L, "Cu/p-Si Schottky photodetectors at 1.55 um," Proc. SPIE 7719, Silicon Photonics and Photonic Integrated Circuits II, 77190R, 2010.

28. Zhu, S., Yu1, M. B., Lo, G. Q., and Kwong, D. L., "Near-infrared waveguide-based nickel silicide Schottky-barrier photodetector for optical communications," *Appl. Phys. Lett.* 92, 081103,2008.

29. Ghioni, M., Gulinatti, M., Rech, I., Zappa, F., and Cova, S., "Progress in Silicon Single-Photon Avalanche Diodes," *IEEE J. Sel. TOPICS In Quantum Elec.* 13, pp. 852–862, 2007.

30. Haitz, R.H., "Mechanisms contributing to the noise pulse rate of avalanche diodes," J. Appl. Phys. 36 pp. 3123–3131, 1965.

31. Lee, M. J., Rücker, H., and Choi, W.Y., "Effects of Guard-Ring Structures on the Performance of Silicon Avalanche Photodetectors Fabricated With Standard CMOS Technology," *IEEE ELECTRON DEVICE Lett.*, 33, pp.80-82, 2012

32. McIntyre, R.J., "Recent developments in silicon avalanche photodiodes," *Measurement*, 3: pp. 146 – 152. 1985.

33. Dautet, H., Deschamps, P., Dion, B., Macgregor , A.D., Macsween, D., McIntyre, R.J., Trottier, C., and Webb, P.P., "Photon counting techniques with silicon avalanche photodiodes," *J. Appl. Opt.* 32, pp. 3894 – 3900, 1993.

34. Spinelli, A., Ghioni, M., Cova S., and Davis, L.M. ,"Avalanche Detector with Ultraclean Response for Time-Resolved Photon Counting," *IEEE J. Quantum Electron.* 34, pp.817 – 821, 1998.

35. Hart, T. R., Aggarwal, R. L., and Lax, B., "Temperature Dependence of Raman Scattering in Silicon," *Phys. Rev. B.* 1, pp. 638- , 1970.

36. Gummel, H., and Lax, M., "Thermal capture of electrons in silicon," *Annals of Physics*, 2, pp. 28-56, 1957.

37. Murari, K, Etienne-Cummings, R., Thakor, N., and Cauwenberghs, G., "Which photodiode to Use: A comparison of COMS-Compatible Structures," *IEEE Sensors Journal*, 9, pp.752-760, 2009.

38. Murari, K, Etienne-Cummings, R., Thakor, N., and Cauwenberghs, G., "A CMOS In-Pixel CTIA high sensitivity fluorescence imager," *IEEE Trans Biomed Circuits Syst*. 5, pp. 449-458, 2011.

39. Biber, A., Seitz, P., and Jackel, H., "Avalanche Photodiode image sensor in standard BiCMOS technology," *IEEE Transactions on Electron Devices,* 47, pp. 2241-2243, 2000.

40. Xu, R., Liu, B., and Yuan, J., "A 1500 fps highly sensitive 256×256 CMOS imaging sensor with in-pixel calibration," *IEEE Journal of Solid-State Circuits*, 47, pp. 1408-1418, 2012.

41. Fossum, E. R., and Hondongwa, D.B., "A Review of the Pinned Photodiode for CCD and CMOS Image Sensors," *IEEE Journal of the Electron Devices Society*, 2, pp. 33-43, 2014.

42. Cheng, J., You, S., Rahman, S., and Lo, Y. H., "Self-quenching InGaAs/InP single photon avalanche detector utilizing zinc diffusion rings," *Optics Express*, 19, pp. 15149-15154, 2011.

43. Rahman, S. N., Hall, D., and Lo, Y. H., "Non-Geiger mode single photon detector with multiple amplification and gain control mechanisms," *J. Appl. Phys.*115, 173104, 2014.

44. Rahman, S. N., Hall, D., Mei, Z., and Lo, Y. H., "Integrated 1550 nm photoreceiver with built-in amplification and feedback mechanisms," *Opt. Lett.* 38, pp. 4166-4169, 2013.

45. You, S., Cheng, J., and Lo, Y. H., "Physics of Single Photon Avalanche Detectors With Built-In Self-Quenching and Self-Recovering Capabilities," *IEEE Journal of Quantumelectronics*, 48, pp. 960-967, 2012.